

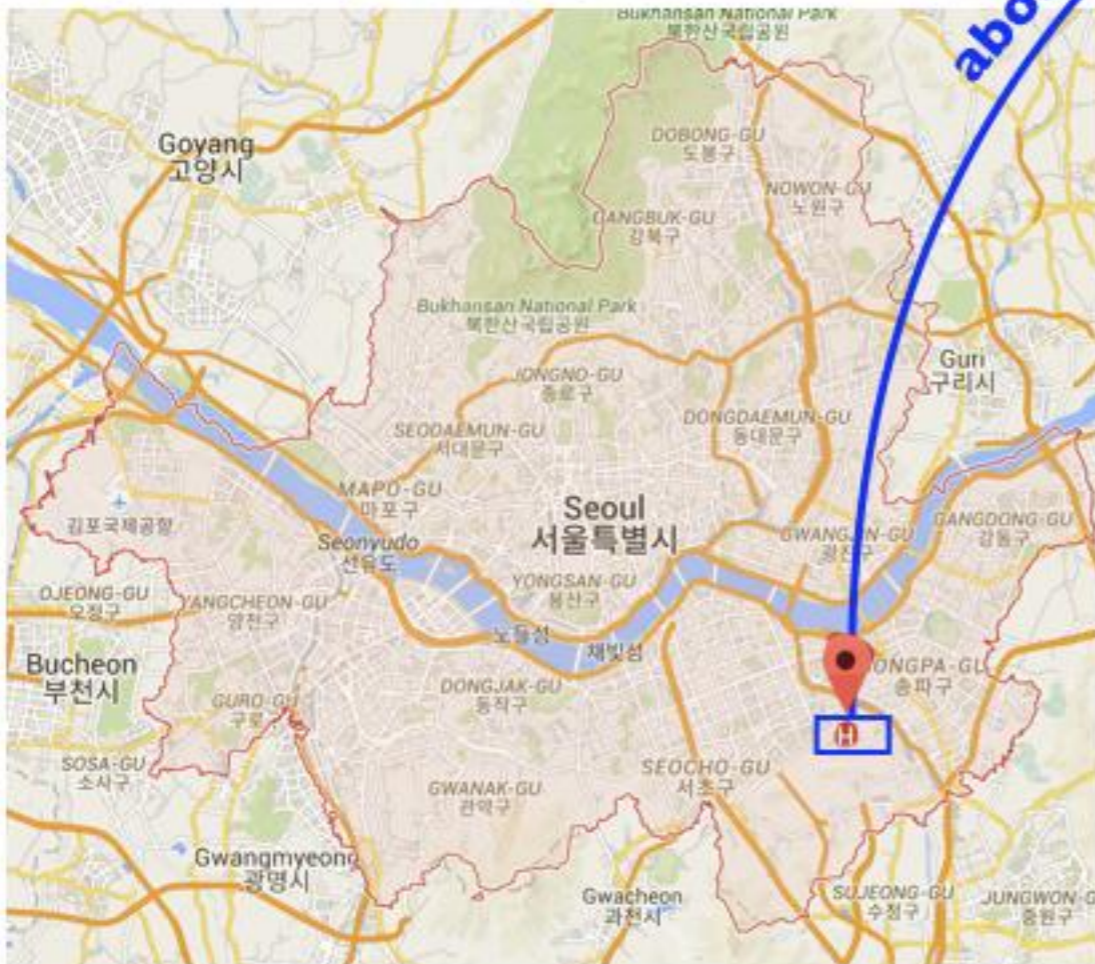
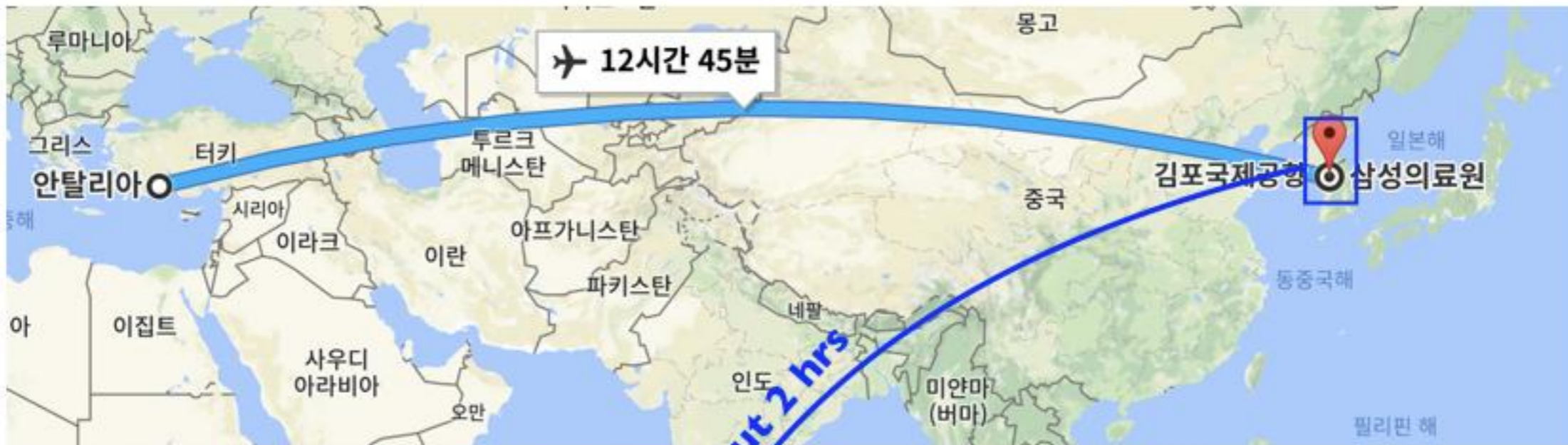
Integration of MRI in Radiotherapy

Sang Hoon Jung, Ph.D,

Clinical Assistant Professor / Medical Physicist
Department of Radiation Oncology, Samsung Medical Center



Location of SMC (Dept. Radiation Oncology)



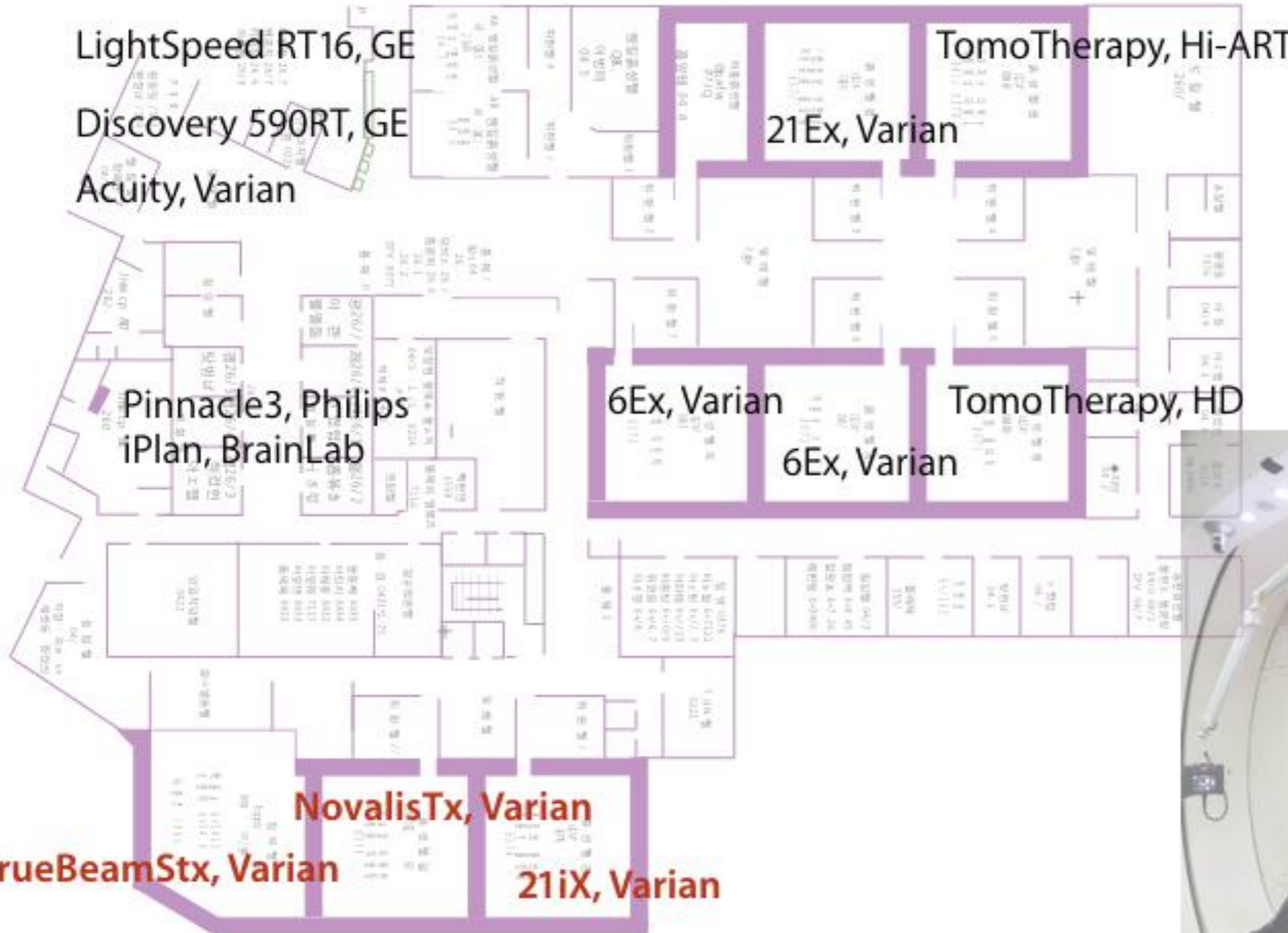
Resources in SMC

			
1994	2002	2008	2016
2 Faculty (MD)	4 Faculty (MD)	6 Faculty (MD)	11 Faculty (MD)
1 Physicist Faculty	1 Physicist Faculty	1 Physicist Faculty	4+5 Physicist Faculty (+2/+7)
			1 Biologist Faculty
	4 Trainee	10 Trainee	8 Trainee (Resid. & fellow)
9 RTT	18 RTT	35 RTT	56 RTT
19	37	68	121



Resources in SMC

Conventional Simulator: 1
 CT simulators: 3
MR-RT simulator: 1
 Linacs: 6
 TomoTherapies: 2
 Gantries with CBCT: 2



Multimodal images in radiotherapy

- A random sample of 1600 radiation oncologists in USA
- 393 responses
- Disease site - modality, delivery techniques.

as of 2009, [%]

	CNS	H/N	Lung	Breast	GI	GYN	GU	L/L	Ped
Target Delineation									
All	79	80	83	20	53	46	44	56	14
MR	68	37	4	4	7	18	33	4	11
PET	15	3	68	10	40	33	8	47	8
4DCT	2	4	37	5	17	3	3	3	2
In-Room Imaging									
All	72	74	67	44	60	58	91	40	24
Video	1	1	0	2	1	1	1	0	1
US	0	0	0	2	1	2	23	0	0
MV 2D	35	33	30	26	27	27	43	22	11
kV 2D	42	37	35	17	28	26	42	17	0
3D	35	38	37	12	33	27	45	15	12

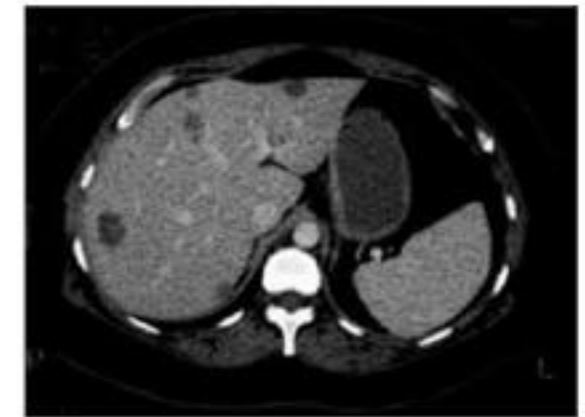
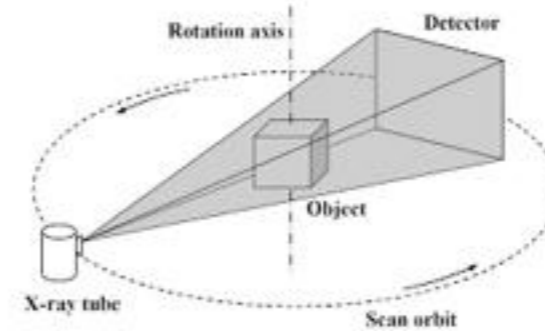
D. R. Simpson, et al., Cancer **116**, 3953-3960 (2010).

D. R. Simpson, et al., JACR **6**, 876-883 (2009).

Multi-modal images in radiotherapy

- Computed Tomography

- Attenuation coefficient
- Energy, imaging protocol, contrast agent



- Positron Emission Tomography

- Positron-emitting radionuclide
- Agent, FDG, MISO, and so on

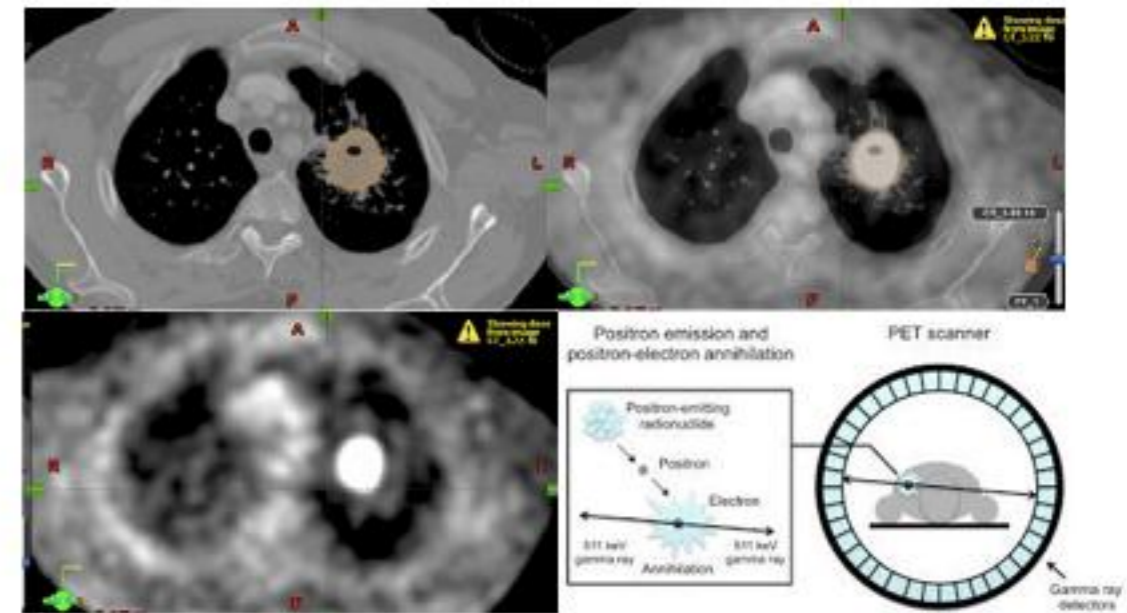
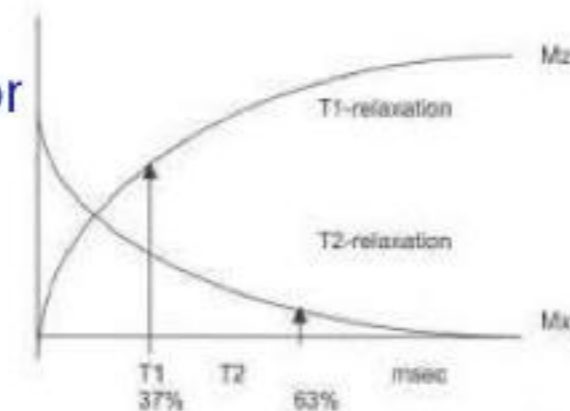


Figure 4 PET/CT fusion role in delineation of tumor. Left: CT image showing gross tumor. Right: PET image showing disease uptake. Middle: PET/CT fusion correlating gross tumor with uptake in PET.

- Magnetic Resonance Imaging

- Resonance pulse, Relaxation time, and so on
- Contrast agent, imaging protocols, and so on



Tissue	T1 (msec)	T2 (msec)
Water/CSF	4000	2000
Gray matter	900	90
Muscle	900	50
Liver	500	40
Fat	250	70
Tendon	400	5
Proteins	250	0.1- 1.0
Ice	5000	0.001

- Ultrasound, etc.

Preliminary image in radiotherapy

- Computed tomography
 - Electron density converted to attenuation coefficient for radiotherapy
 - Geometrical accuracy of anatomy
 - **Lack of contrast resolution for differentiation between normal soft tissue structures and tumor extent**
- Advantages of MRI in radiotherapy
 - Superior contrast resolution and better soft tissue differentiation
 - No need - radiation exposure, iodinated contrast agent
 - Functional imaging sequences

	CT	PET	MRI
Signal intensity	Electron density	Uptake	Material composition and uptake
Resolution	Fine	Coarse	Fine
3D imaging	OK	OK	OK
Radiation	Exposure	Exposure	Non-ionizing
Acquisition time	less than 1 min	mins	a few seconds ~ mins (Imaging protocol)
Anatomy	OK	N/A	OK

History of MRI

- 1952 Herman Carr - Ph.D. Thesis
- 1973 Lauterbur PC

190

microamorphous, and microphasitic, and further on a geometric basis into microgranular, microlamellar, and microfibrillar. More recently, Kloss¹³ reported that, unlike macrocrystalline quartz crystals, microcrystalline quartz crystals generally show no sharp inversion points, and the inversion takes place over an interval of nearly 50° C. Our work suggests that it is best to describe the product of powdering quartz as microcrystalline quartz, which has an X-ray structure corresponding to quartz but is not normally detectable by d.s.a. unless carried out at high heating rates. In addition, this microcrystalline quartz contains chemisorbed H₂O.

We thank Professor R. A. Howie, Mordecai Moses, E. Nave, N. Walsh and Miss P. S. Osborne, and the Science Research Council.

G. S. M. MOORE
H. E. ROSE

Powder Science Laboratory,
Department of Mechanical Engineering,
King's College, Strand,
London WC2

Received October 10, 1972.

- 1 Dempster, P. B., and Ritchie, P. D., *J. Appl. Chem.*, **3**, 182 (1953).
- 2 Hildebrand, W. F., *J. Amer. Chem. Soc.*, **38**, 1120 (1916).
- 3 Keith, M. L., and Tuttle, O. F., *Amer. J. Sci.*, Bowen vol., **303** (1952).
- 4 Ray, R. C., *Proc. Roy. Soc.*, **101**, A, 309 and 640 (1922).
- 5 Sosnas, R. B., and Mervin, H. E., *J. Wash. Acad. Sci.*, **14**, 117 (1924).
- 6 Dale, A. J., *Trans. Brit. Ceram. Soc.*, **23**, 211 (1924).
- 7 Cleland, D. W., and Ritchie, P. D., *J. Appl. Chem.*, **3**, 42 (1952).
- 8 Dempster, P. B., and Ritchie, P. D., *J. Appl. Chem.*, **3**, 187 (1953).
- 9 Sakabe, H., et al., *Bull. Nat. Inst. Indus. Jap.*, **4**, 1 (1960).
- 10 Soda, R., *J. Chem. Soc. Jap.*, **34**, 1491 (1961).
- 11 Sosnas, R. B., *The Physics of Silica*, 218 (Kratzer University Press, 1945).
- 12 Strydom-Kloss, W., *Contr. Mineral. Petrol.*, **36**, 1 (1972).

Image Formation by Induced Local Interactions: Examples Employing Nuclear Magnetic Resonance

An image of an object may be defined as a graphical representation of the spatial distribution of one or more of its properties. Image formation usually requires that the object interact with a matter or radiation field characterized by a wavelength comparable to or smaller than the smallest features to be distinguished, so that the region of interaction may be restricted and a resolved image generated.

This limitation on the wavelength of the field may be removed, and a new class of image generated, by taking advantage of induced local interactions. In the presence of a second field that restricts the interaction of the object with the first field to a limited region, the resolution becomes independent of wavelength, and is instead a function of the ratio of the normal width of the interaction to the shift produced by a gradient in the second field. Because the interaction may be regarded as a coupling of the two fields by the object, I propose that image formation by this technique be known as zeugmatography, from the Greek ζεύγωμα, "that which is used for joining".

The nature of the technique may be clarified by describing two simple examples. Nuclear magnetic resonance (NMR) zeugmatography was performed with 60 MHz (5 m) radiation and a static magnetic field gradient corresponding, for proton resonance, to about 700 Hz cm⁻¹. The test object consisted of two 1 mm inside diameter thin-walled glass capillaries of H₂O attached to the inside wall of a 4.2 mm inside diameter glass tube of D₂O. In the first experiment, both capillaries contained pure water. The proton resonance line width, in the absence of the transverse field gradient, was about 5 Hz.

NATURE VOL. 242 MARCH 16 1973

Assuming uniform signal strength across the region within the transmitter-receiver coil, the signal in the presence of a field gradient represents a one-dimensional projection of the H₂O content of the object, integrated over planes perpendicular to the gradient direction, as a function of the gradient coordinate (Fig. 1). One method of constructing a two-dimensional projected image of the object, as represented by its H₂O content, is to combine several projections, obtained by rotating the object about an axis perpendicular to the gradient direction (or, as in Fig. 1, rotating the gradient about the object), using one of the available methods for reconstruction of objects from their projections¹⁻³. Fig. 2 was generated by an algorithm, similar to that of Gordon and Herman⁴, applied to four projections, spaced as in Fig. 1, so as to construct a 20 × 20 image matrix. The representation shown was produced by shading within contours interpolated between the matrix points, and clearly reveals the locations and dimensions of the two columns of H₂O. In the second experiment, one capillary contained pure H₂O, and the other contained a 0.19 mM solution of MnSO₄ in H₂O. At low radio-frequency power (about 0.2 mW) the two capillaries gave nearly identical images in the

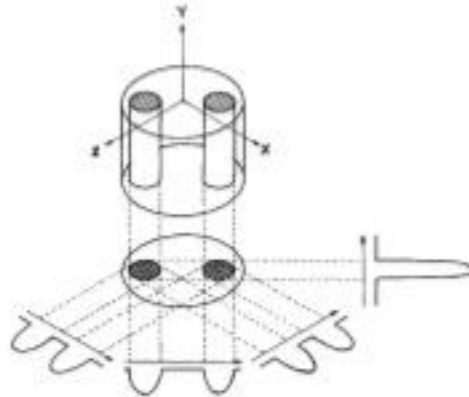


Fig. 1 Relationship between a three-dimensional object, its two-dimensional projection along the Y-axis, and four one-dimensional projections at 45° intervals in the XZ-plane. The arrows indicate the gradient directions.



Fig. 2 Proton nuclear magnetic resonance zeugmatogram of the object described in the text, using four relative orientations of object and gradients as diagrammed in Fig. 1.

NATURE VOL. 242 MARCH 16 1973

zeugmatogram (Fig. 3a). At a higher power level (about 1.6 mW), the pure water sample gave much more saturated signals than the sample whose spin-lattice relaxation time T_1 had been shortened by the addition of the paramagnetic Mn²⁺ ions, and its zeugmatographic image varied as the contour level used in Fig. 3a. The sample region with long T_1 may be selectively emphasized (Fig. 3c) by constructing a difference zeugmatogram from those taken at different radio-frequency powers.

Applications of this technique to the study of various inhomogeneous objects, not necessarily restricted in size to those commonly studied by magnetic resonance spectroscopy, may be anticipated. The experiments outlined above demonstrate the ability of the technique to generate pictures of the distributions of stable isotopes, such as H and D, within an object. In the second experiment, relative intensities in an image were made to depend upon relative nuclear relaxation times. The variations in water contents and proton relaxation times among biological tissues should permit the generation, with field gradients large compared to internal magnetic inhomogeneities, of useful zeugmatographic images from the rather sharp water resonances of organisms, selectively picturing the various soft structures and tissues. A possible application of considerable interest at this time would be to the *in vivo* study of malignant tumours, which have been shown to give proton nuclear magnetic resonance signals with much longer water spin-lattice relaxation times than those in the corresponding normal tissues⁵.

The basic zeugmatographic principle may be employed in many different ways, using a scanning technique, as described above, or transient methods. Variations on the experiment, to be described later, permit the generation of two- or three-dimensional images displaying chemical compositions, diffusion coefficients and other properties of objects measurable by spectroscopic techniques. Although applications employing nuclear magnetic resonance in liquid or liquid-like systems are simple and attractive because of the ease with which field gradients large enough to shift the narrow resonances by many

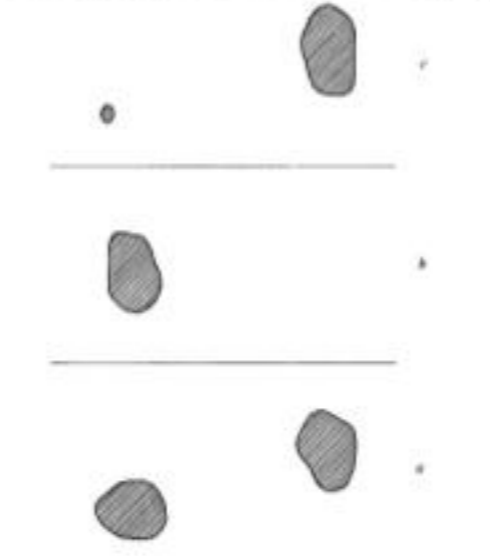


Fig. 3 Proton nuclear magnetic resonance zeugmatograms of an object containing regions with different relaxation times. a, Low power; b, high power; c, difference between a and b.

NATURE VOL. 242 MARCH 16 1973

line widths may be generated, NMR zeugmatography of solids, electron spin resonance zeugmatography, and analogous experiments in other regions of the spectrum should also be possible. Zeugmatographic techniques should find many useful applications in studies of the internal structures, states, and compositions of microscopic objects.

P. C. LAUTERBUR

Department of Chemistry,
State University of New York at Stony Brook,
Stony Brook, New York 11790

Received October 30, 1972; revised January 8, 1973.

- 1 Bracewell, R. N., and Riddle, A. C., *Astronomy J.*, **158**, 427 (1967).
- 2 Vainstein, L. K., *Soviet Physics-Crystallography*, **15**, 781 (1971).
- 3 Ramchandran, G. N., and Lakshminarayana, A. V., *Proc. US Nat. Acad. Sci.*, **68**, 2236 (1971).
- 4 Gordon, R., and Herman, G. T., *Comm. Assoc. Comput. Mach.*, **14**, 759 (1971).
- 5 Klug, A., and Crowther, R. A., *Nature*, **238**, 435 (1972).
- 6 Weisman, I. D., Beron, L. H., Maxwell, Sr., L. R., Woods, M. W., and Burk, D., *Science*, **178**, 1288 (1972).

BIOLOGICAL SCIENCES

Island Lizards: the Genetic-Phenetic Variation Correlation

NATURAL populations of many organisms are known to contain much more genetic variation than would have been predicted by all but a minority¹ of geneticists two decades ago. Individuals of several species have up to 22% of their loci heterozygous, and from 0-50% or more of the loci in a population are polymorphic, although the higher estimates may result from sampling error²⁻⁴; vertebrates tend to be at the lower end of these ranges. Estimates such as these are based on electrophoretically detectable variation in proteins, so the true levels of genetic variation are probably higher⁵. These generalizations are gaining wide acceptance, but there is still some unease about their accuracy. The fundamental question is whether the loci being sampled are representative of the genome as a whole. We here present evidence that the electrophoretic approach is relatively unbiased.

Two groups of lizards were used: eight species of *Anolis* from the West Indies and thirteen populations of the side-notched lizard *Uta stansburiana*, *sensu lato*, from California and Mexico, caught in 1971 and 1972. Geographic variation is not a source of heterogeneity, as all specimens from a locality were collected within a few hundred metres of one another. After capture, they were transported alive or on dry ice to the laboratory and stored at -70° C until needed. After skinning, water-soluble proteins were routinely extracted and electrophoresed⁶. Six of the eight *Anolis* species were from Puerto Rico, and two, *A. eximius* and *A. rugosus*, were from Barbados and Martinique, respectively.

A single morphological character was used to estimate morphological variation in the *Anolis* species; the number of subdigital scales on the longest toe (second) on the hind foot, starting with the most distal lamella and counting proximally. Variability in this character is correlated with variability in other scale characters, but the other characters were not scored as accurately. Estimates of genetic variation in the *Anolis* species were derived from the starch-gel electrophoresis patterns of enzymes and nonenzymatic proteins, which together appear to represent the gene products of twenty-one or twenty-two loci. The proteins assayed were lactate dehydrogenase, malate dehydrogenase, α-glycerol-phosphate dehydrogenase, isocitrate dehydrogenase, indophenol oxidase, phosphoglucose isomerase, phosphoglutamase, glutamic oxaloacetate

History - Integration of MRI into radiotherapy

- Initial reports in radiotherapy
 - Fabrikant JI, et al.(1985), Heavy charged-particle Bragg peak radiosurgery for intracranial vascular disorders.
 - HoudekPV, et al. (1989), MR technique for localization and verification procedures in episcleral brachytherapy.
- Fraass BA, et al (1987): **Integration of magnetic resonance imaging into radiation therapy treatment planning: I. Technical considerations**
 - mechanically-obtained external contour and simulator film data,
 - The study has shown that to use MRI data for RTTP,
 - (a) **use careful patient positioning and marking,**
 - (b) transfer information from CT to MRI and vice versa,
 - (c) determine the **geometrical consistency** between the CT and MR data sets,
 - (d) investigate the **unwarping of distorted MR images,** and
 - (e) have the ability to **use non-axial images** for determination of beam treatment technique, dose calculations, and plan evaluation.

History - Integration of MRI into radiotherapy

- MRI simulator
 - T. Mizowaki et al., 1996 (Kyoto University)
 - **0.2T permanent magnet system (Open type)**
 - **Off-axis 10 cm < geometrical error of 2 mm**
 - Clinical output and effectiveness for bone metastases (2001)
- MRI based Treatment planning for prostate cancer (L. Chen et al., PMB, 2004)

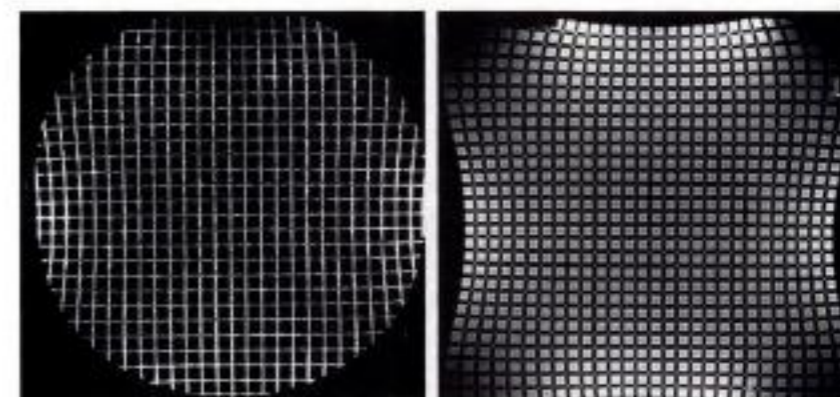


Figure 4. MR images of the two types of phantom. (a) T1-weighted axial images of the cylindrical phantom (FOV, 260 mm). (b) T1-weighted axial images of the cube-shaped phantom (FOV, 320 mm). Geometric distortion was generally observed in the peripheral area of the images. L = left.

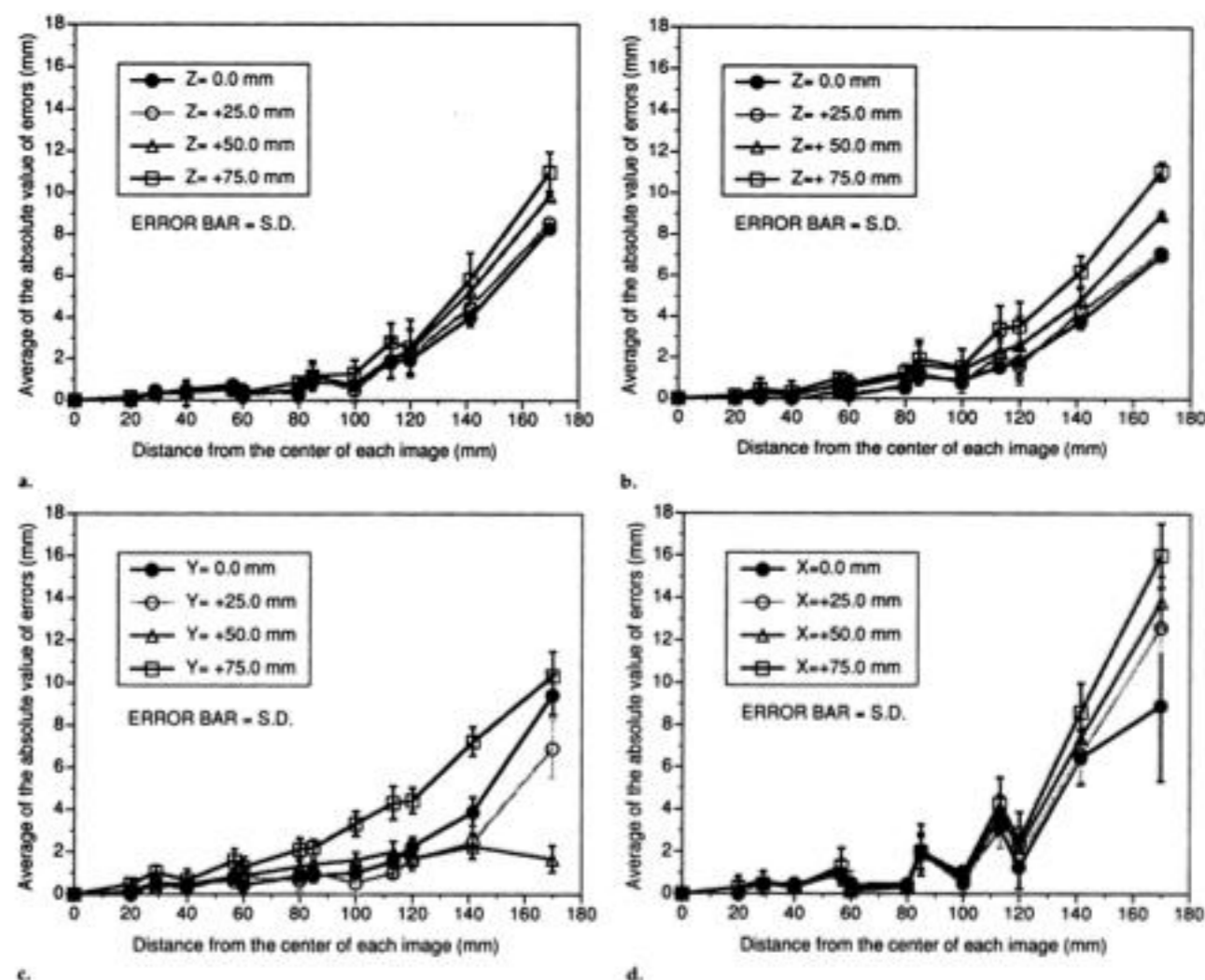
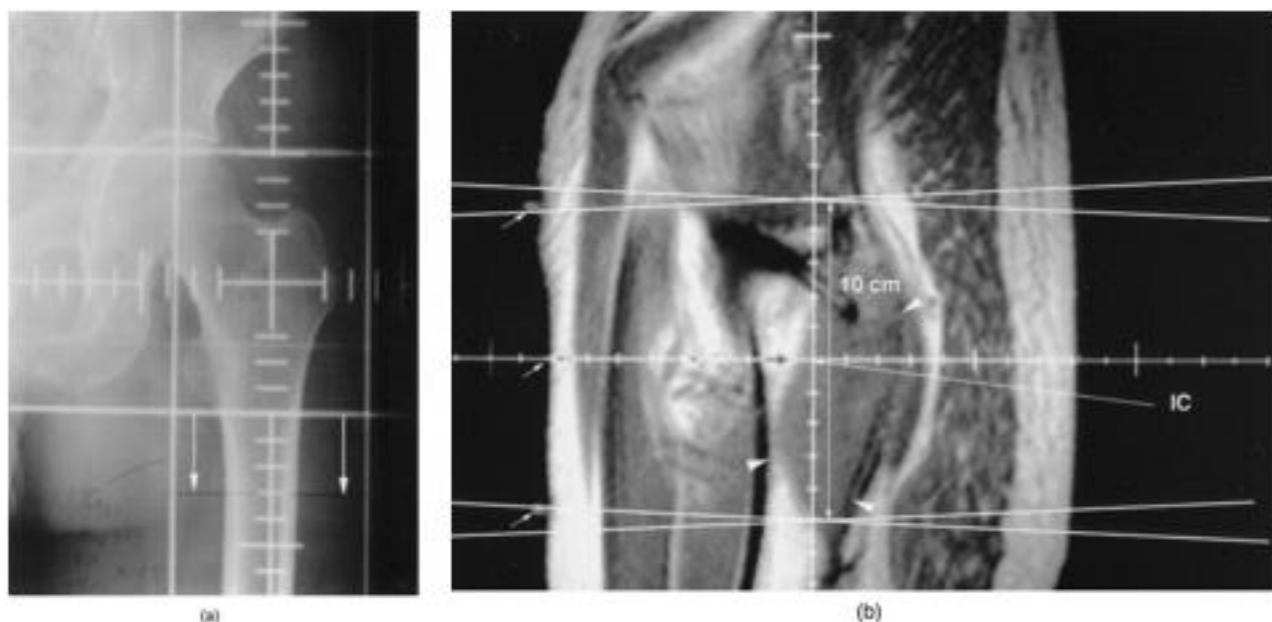


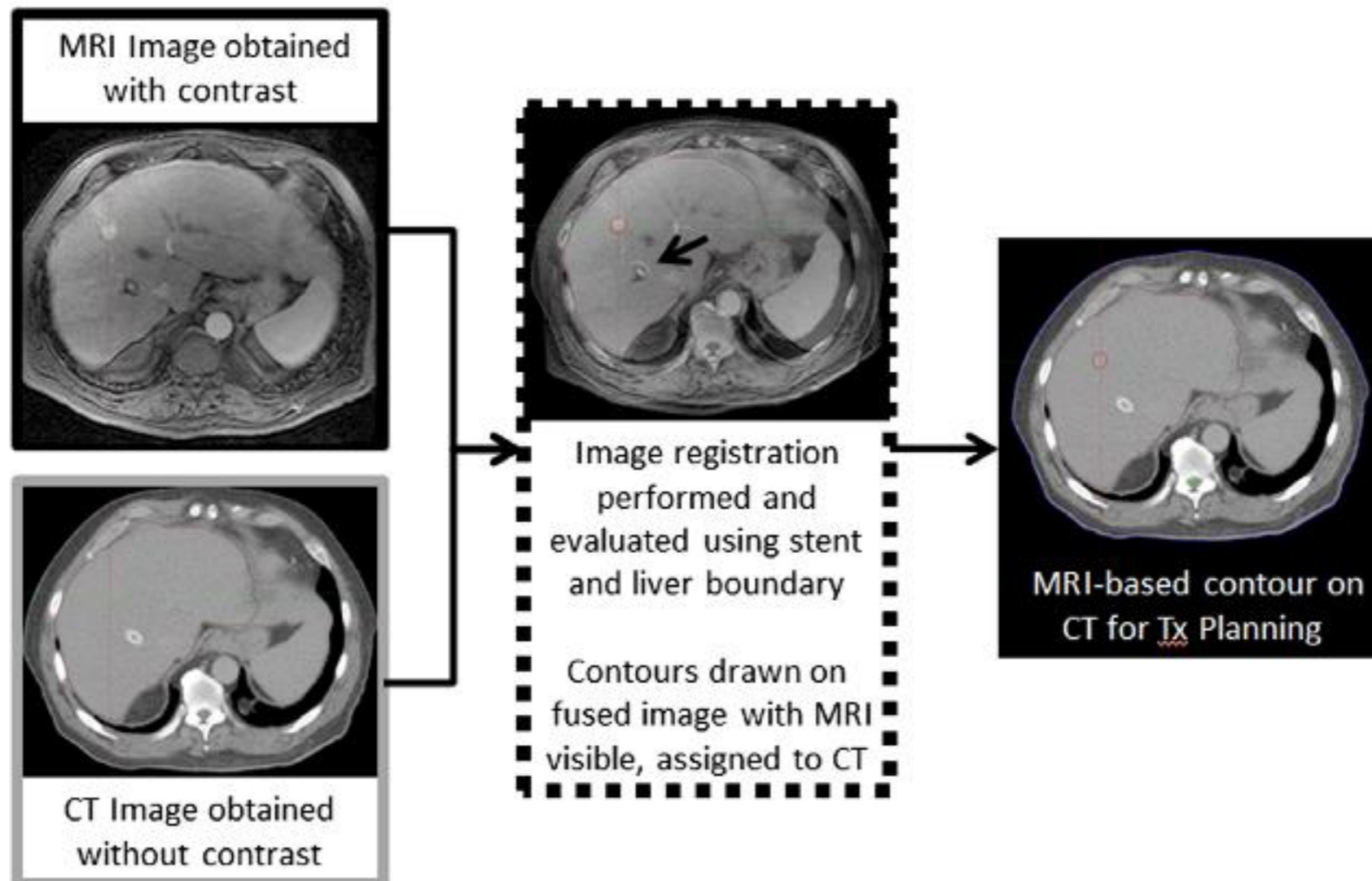
Figure 5. Positional errors in (a) T1-weighted axial, (b) T2-weighted axial, (c) T1-weighted coronal, and (d) T1-weighted sagittal MR images. Almost all positional errors within the 100-mm radius from the center of the image were within 2 mm. S.D. = standard deviation, X = coordinate of the x axis, perpendicular to the sagittal sections. Coordinates on the left side of the center are indicated by +. Y = coordinate of the y axis, perpendicular to the coronal sections. Coordinates on the upper side of the center are indicated by +. Z = coordinate of the z axis, perpendicular to the axial sections. Coordinates on the cranial side of the center are indicated by +.



T. Mizowaki, Y. Nagata, K. Okajima, R. Murata, M. Yamamoto, M. Kokubo, M. Hiraoka and M. Abe, "Development of an MR simulator: experimental verification of geometric distortion and clinical application," *Radiology* **199**, 855-860 (1996).

MRI Integration in a CT-Based Radiotherapy Workflow

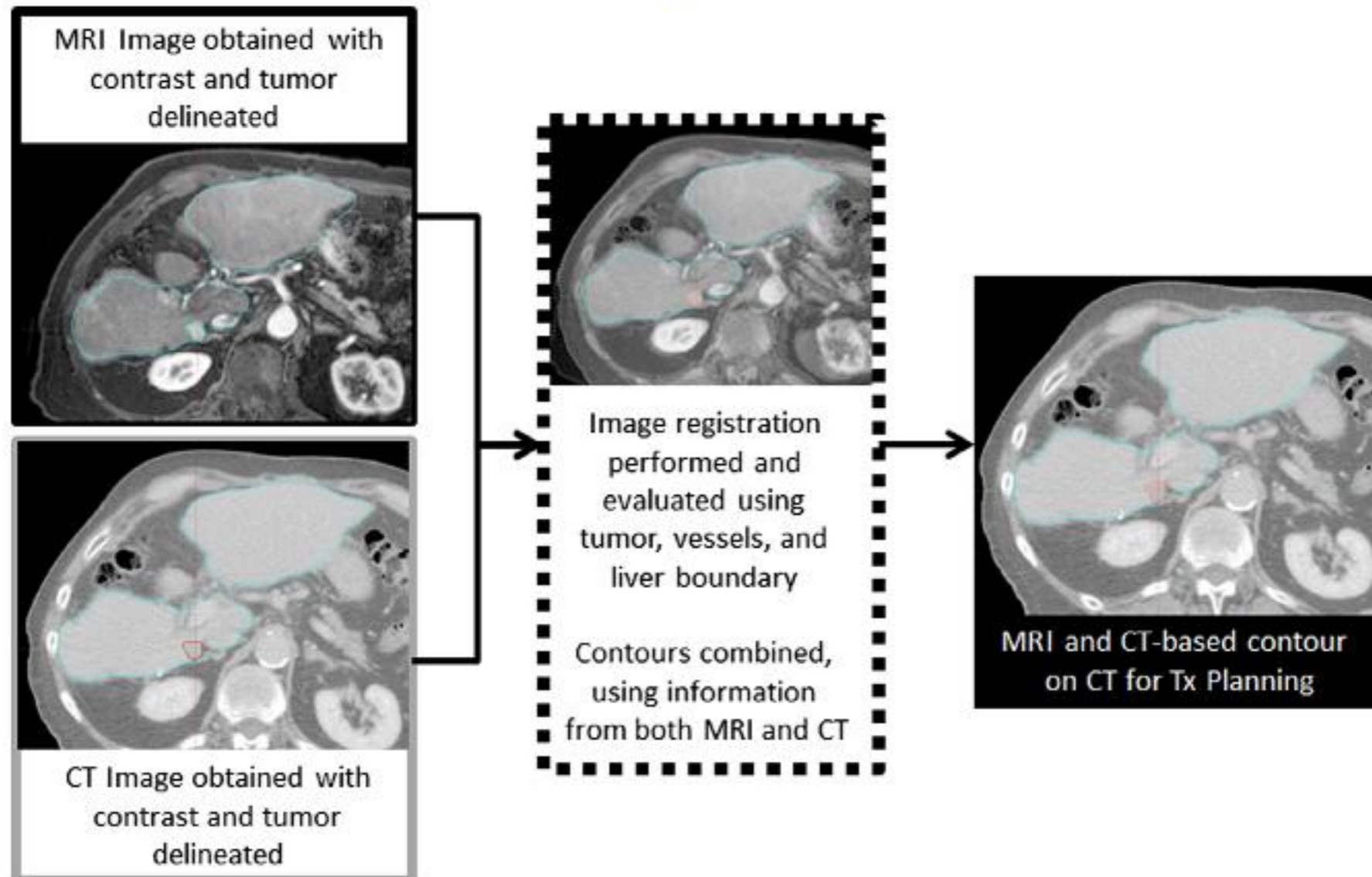
- Strategy I, Non contrast CT + contrast MRI
- Target delineation
- Visible outline of organ or landmark



K. K. Brock and L. A. Dawson, Seminars in Radiation Oncology **24**, 169-174 (2014).

MRI Integration in a CT-Based Radiotherapy Workflow

- Strategy II, contrast CT + contrast MRI
- Target delineation
- Visible outline of organ or landmark



K. K. Brock and L. A. Dawson, Seminars in Radiation Oncology **24**, 169-174 (2014).

MRI Integration in a CT-Based Radiotherapy Workflow

- Accuracy of registration is the most important.

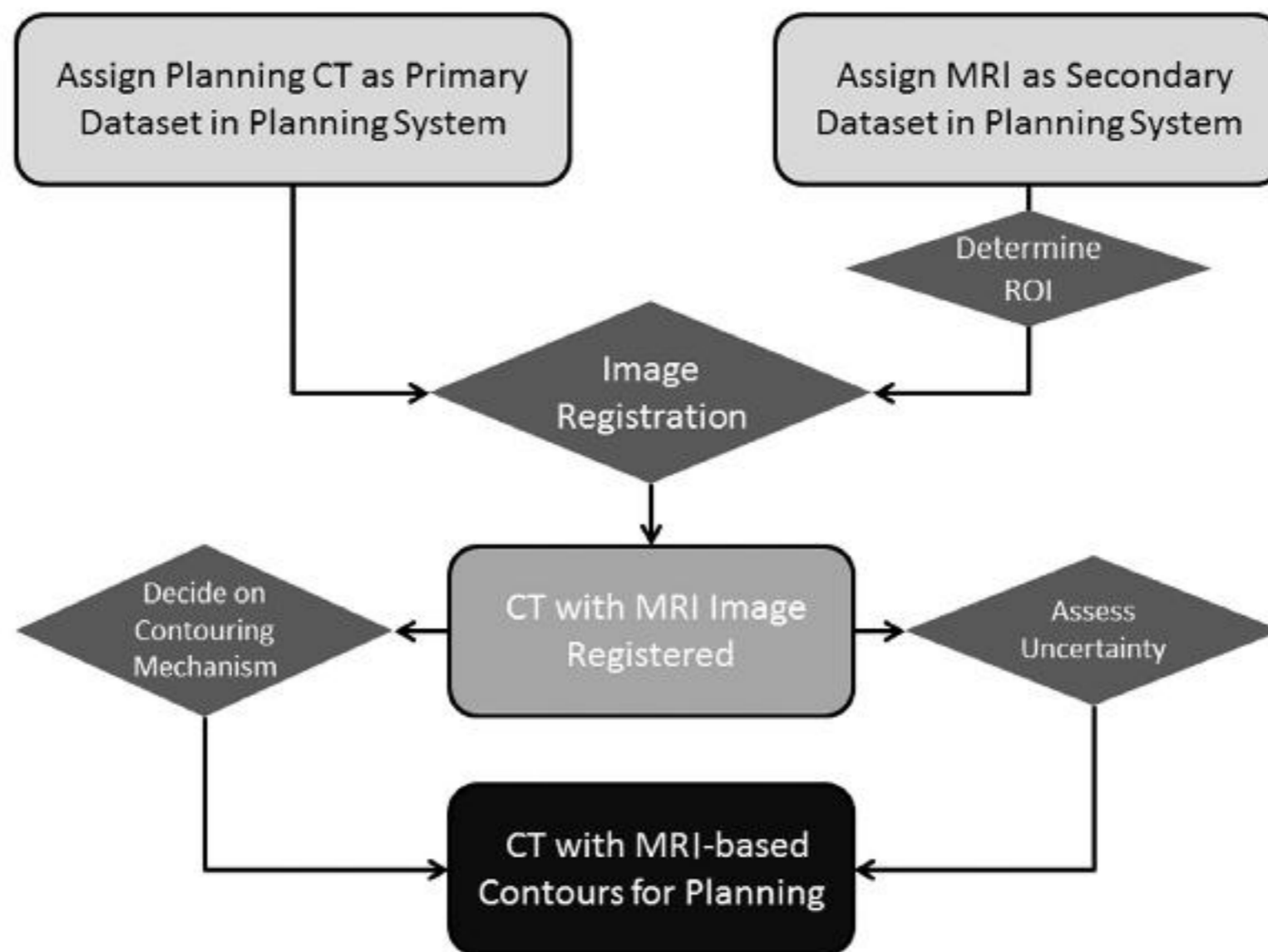


Figure 1 Overall workflow for integrating MRI into a CT-based treatment planning process.

K. K. Brock and L. A. Dawson, *Seminars in Radiation Oncology* **24**, 169-174 (2014).

Challenge: Generation of Synthetic CT

Unit Density

- The entire patient anatomy as a single bulk density, typically that of water or a mixture of adipose and muscle tissue
- Mean dose discrepancy less than 3%

Brain tumor

Gamma Knife radiosurgery

CT with heterogenous correction

CT without heterogenous correction

MRI with HU of 0

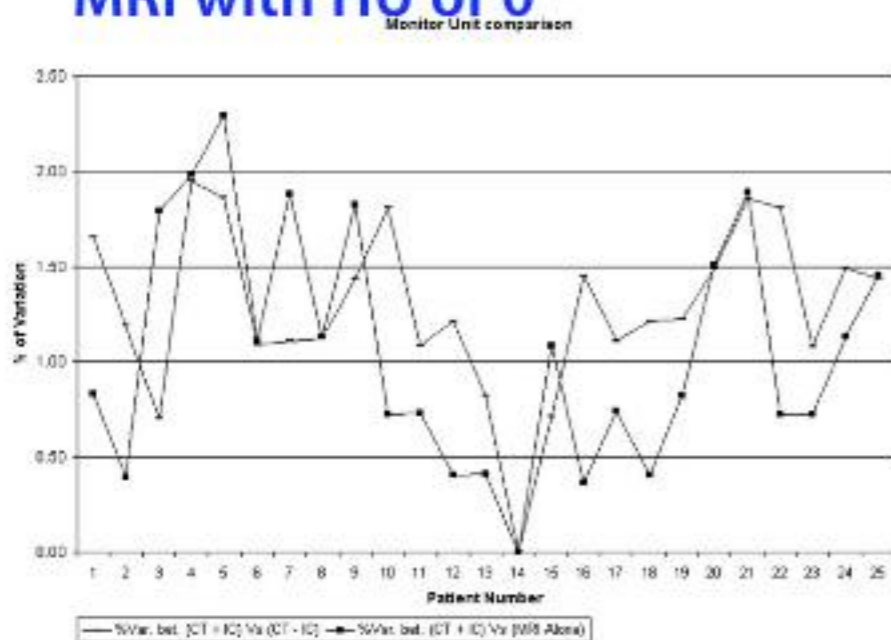


Figure 3. Monitor unit variation of CT without inhomogeneity and MRI alone with respect to CT with inhomogeneity. Var. bet, variation between; IC, inhomogeneity correction.

Comparison of mean value for different dosimeter parameters

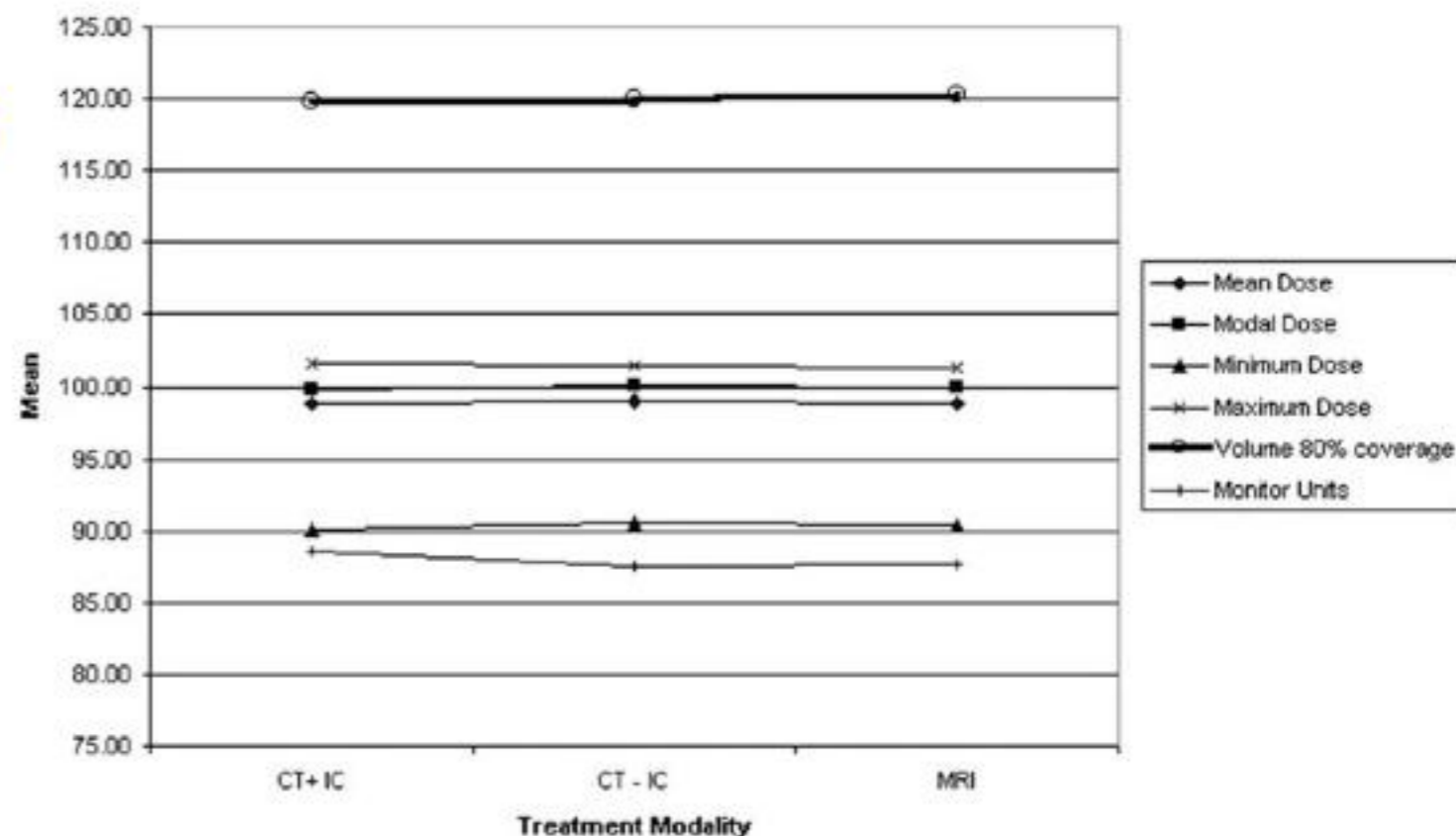


Figure 4. Comparison of mean value for different dosimetric parameters.

Bulk Density with Bone

- Manual Bulk Density Assignment
 - The entire patient anatomy as a single bulk density, typically that of water or a mixture of adipose and muscle tissue
- Mean dose discrepancy less than 3%
- Different bulk density
 - Intracranial <1%

Table 4

Mean percentage point dose differences between the CT density corrected dose calculation and dose calculations based on unit density and bulk density, bone segmented mediums

Photon energy (MV)	Medium	Dose points			
		Isocenter	Norm	CT tumour center	MR tumour center
4	Unit density	1.5 ± 0.3	1.5 ± 0.3	1.2 ± 0.5	1.2 ± 0.4
	Bulk density (bone)	0.5 ± 0.2	0.3 ± 0.2	0.2 ± 0.4	0.2 ± 0.3
8	Unit density	1.0 ± 0.2	1.0 ± 0.3	1.1 ± 0.4	1.1 ± 0.5
	Bulk density (bone)	0.1 ± 0.1	0.2 ± 0.2	0.3 ± 0.3	0.3 ± 0.3
All	Unit density	1.4 ± 0.4	1.2 ± 0.3	1.2 ± 0.5	1.2 ± 0.4
	Bulk density (bone)	0.4 ± 0.3	0.3 ± 0.2	0.2 ± 0.4	0.2 ± 0.3

B. H. Kristensen, et al., Radiother Oncol **87**, 100-109 (2008).

Bulk Density with Bone

- Manual Bulk Density Assignment
 - The entire patient anatomy as a single bulk density, typically that of water or a mixture of adipose and muscle tissue
- Mean dose discrepancy less than 3% (Unit density), 1.5% (Bulk with Bone)

Prostate cancer

Pinnacle³ and Eclipse

Four or Five Fields with 18 MV

CT with bone, MR with bone

CT uniform density - HU of 0

MRI uniform density - HU of 0

Table 3

Summary of average point dose results for the four bulk electron density plans. The mean dose is the dose per fraction delivered by the plan, and the difference between this value and the full density CT plan is given as a percentage of the target dose delivered by the full density CT plan (200 cGy per fraction).

Plan	Mean dose (cGy)	% Variation from full density CT	Standard deviation (cGy)
CT-based with bone	200.2	+0.1	1.2 (0.6%)
MR-based with bone	197.5	-1.3	1.6 (0.8%)
CT-based, uniform density	197.2	-1.4	1.7 (0.9%)
MR-based, uniform density	194.8	-2.6	1.7 (0.9%)

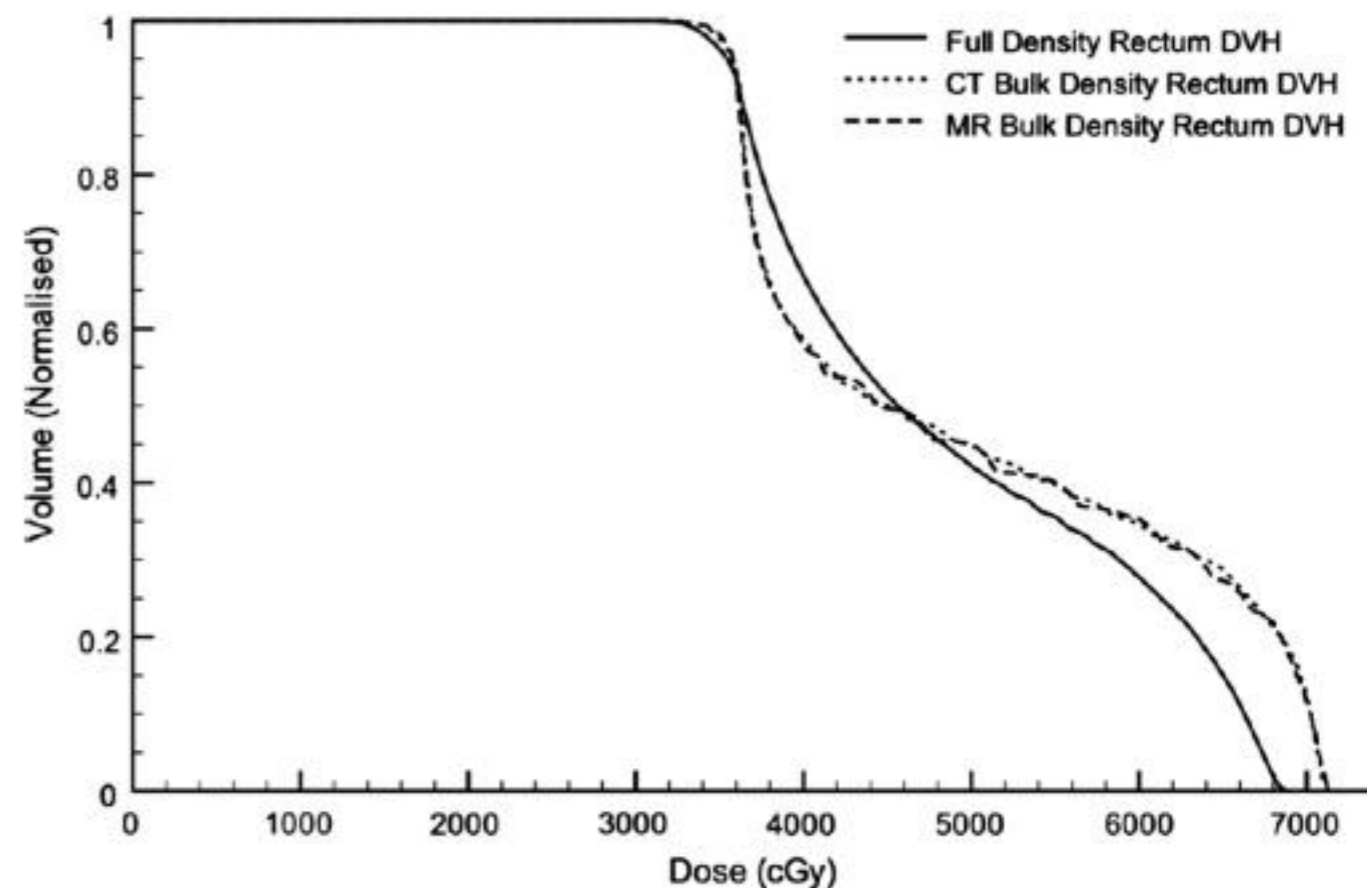


Fig. 1. Comparison of rectum DVHs from the bulk electron density plans to a full density CT plan when large gas pockets are present in the rectum.

Bulk Density with Bone

- Manual Bulk Density Assignment
 - The entire patient anatomy as a single bulk density, typically that of water or a mixture of adipose and muscle tissue
- Mean Dose Discrepancy in Bone density, 1.3 g/cm³)
 - 0.2% for CTV, 4.1% for Bladder, and 5.3% for Rectum

Table I. Dose statistics for the CTV, bladder and rectum that shows the relative differences between clinically approved dose distribution (DD_{DP}) and the dose distributions based upon simulated MR images, DD_W , $DD_{W+B1.3}$, $DD_{W+B2.1}$ (refer to text for details). Prescribed target dose was 50 Gy.

Pat. no.	CTV							Bladder			Rectum				
	Volume [cm ³]	Rel. diff. min. dose [%]			Rel. diff. mean. dose [%]			Volume [cm ³]	Rel. diff. max. dose [%]			Volume [cm ³]	Rel. diff. max. dose		
		DD_W	$DD_{W+B1.3}$	$DD_{W+B2.1}$	DD_W	$DD_{W+B1.3}$	$DD_{W+B2.1}$		DD_W	$DD_{W+B1.3}$	$DD_{W+B2.1}$		DD_W	$DD_{W+B1.3}$	$DD_{W+B2.1}$
1	88.0	-2.2	-1.1	-5.2	-1.0	0.5	5.8	64.2	3.8	3.9	7.5	84.9	4.2	4.9	8.5
2	123.0	-2.7	-2.0	-3.0	-0.7	0.0	2.5	219.8	9.6	9.6	9.5	53.7	7.2	7.4	8.6
3	141.2	-2.4	-1.6	-4.6	-0.9	0.2	4.2	127.2	7.0	7.2	8.6	88.6	5.9	6.2	8.1
4	139.7	-3.4	-2.0	-5.6	-1.2	0.2	4.9	113.2	1.5	1.9	8.8	94.8	5.8	6.3	8.3
5	146.2	-2.0	-1.4	-5.3	-0.7	0.2	3.6	72.1	3.3	3.4	4.6	78.9	5.5	6.9	12.2
6	125.9	-2.7	-1.6	-3.3	-0.7	0.2	3.4	88.5	3.4	3.6	4.7	122.3	4.6	5.3	9.3
7	99.8	-3.1	-1.8	-4.1	-1.3	0.1	5.5	232.0	2.2	2.2	11.0	64.2	4.3	5.0	9.7
8	107.1	-3.4	-1.5	-0.4	-0.8	0.3	4.4	58.6	2.5	2.6	5.2	56.6	-3.6	2.6	5.1
9	185.5	-3.4	-2.2	-5.4	-1.1	0.2	5.2	54.8	2.5	2.4	5.0	76.2	2.4	2.4	9.0
10	185.0	-2.4	-1.2	-6.3	-0.8	0.0	2.9	61.8	4.4	4.4	5.2	60.5	5.2	5.9	8.9
Avg.	134.1	-2.8	-1.6	-4.3	-0.9	0.2	4.2	109.2	4.0	4.1	7.0	78.0	4.2	5.3	8.8
Std.dev.		0.5	0.4	1.7	0.2	0.2	1.1		2.5	2.5	2.3	21.0	3.0	1.7	1.8
Population based mean		-2.7	-1.6	-4.3	-0.9	0.2	4.2		4.0	4.1	7.0		4.2	5.3	8.8

Atlas based synthetic CT

- Atlas based synthetic CT (or pseudo CT)
 - Atlas-based Segmentation on MR images
 - Generating New synthetic CT image from Average CT image
 - 1.5T, T2 FSE, GRE, FSE (Whole pelvis)
 - Five fields with nominal energy of 18MV
 - Dosimetric discrepancy < 2%

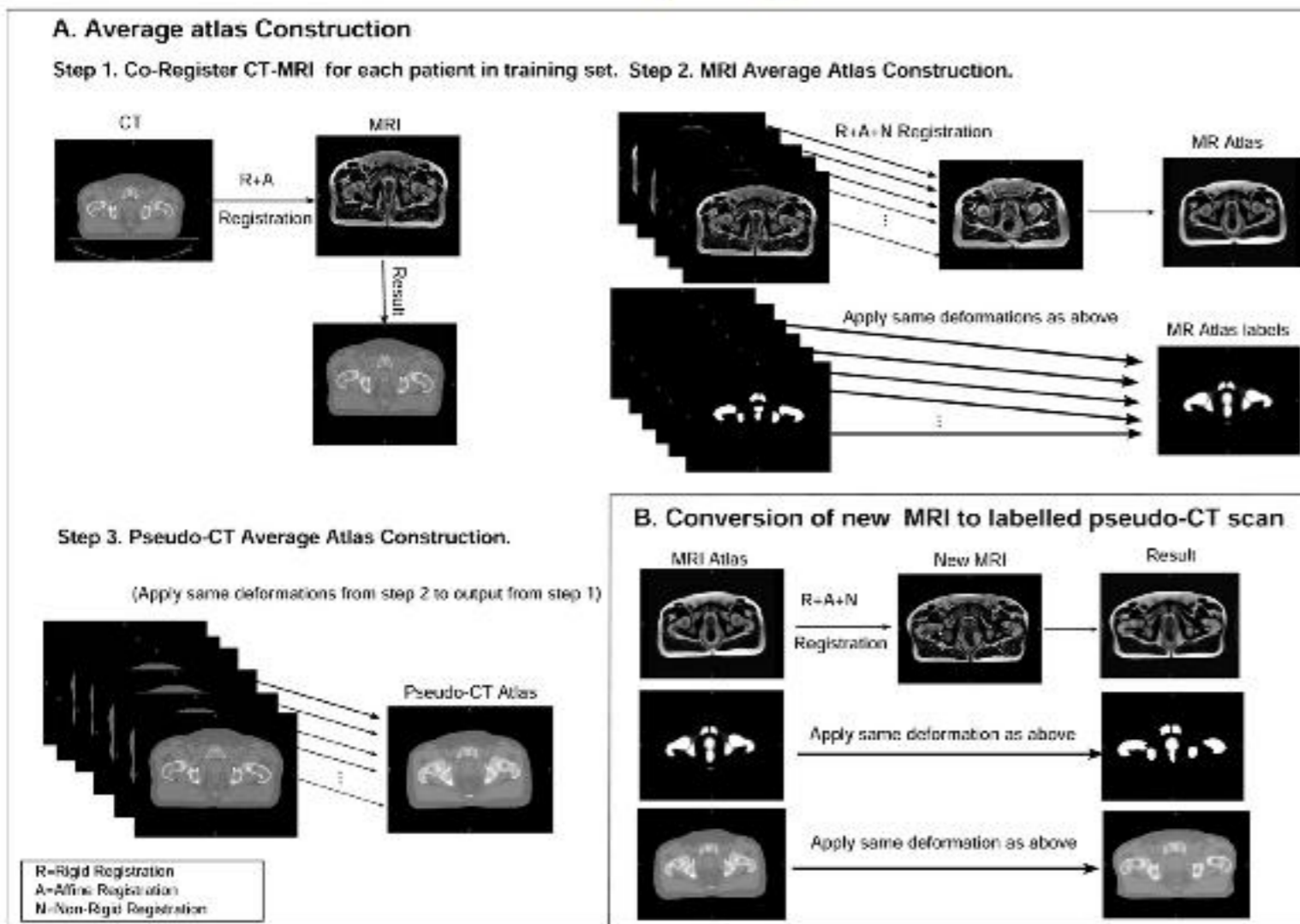


Table 2 Comparison of original CT and pseudo-CT-based HU ($n = 39$)*

Site	CT mean HU (\pm SD)	Pseudo-CT mean HU (\pm SD)	Two-tailed t -test p value result
Rectum	-54 (4)	-54 (143)	>0.9
Bladder	9 (0)	9 (6)	>0.9
Bone	339 (10)	340 (85)	>0.9
Prostate	42 (1)	42 (25)	>0.9

* The increased standard deviation (SD) in the pseudo-CT is due to the large number of CT scans used to generate the pseudo-CT atlas.

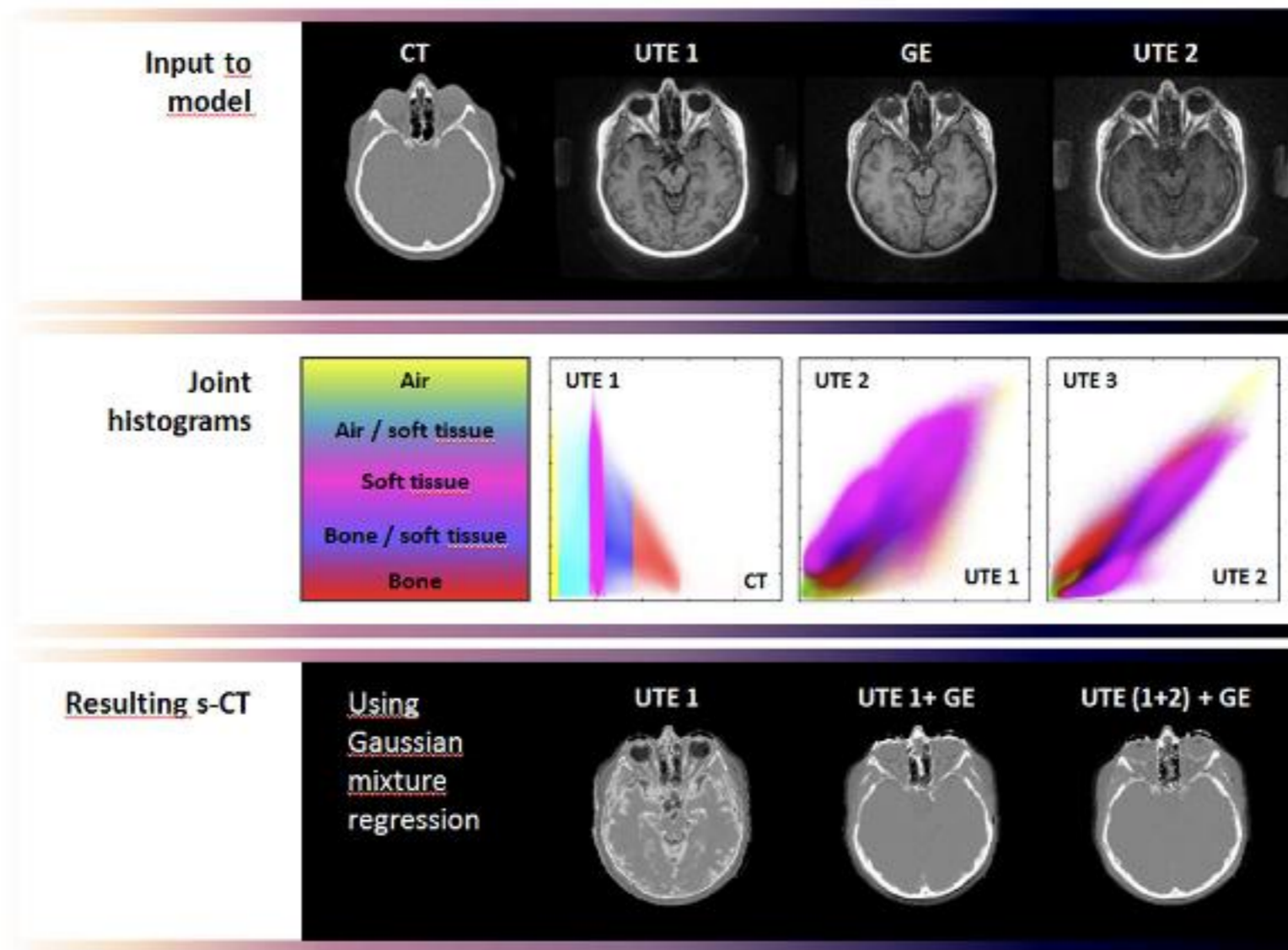
Table 3 Dice similarity coefficient overlapping scores between manual and automatic segmentations for each pelvic organ ($n = 39$)

Site	Mean DSC (\pm SD)
Bone	0.79 (0.12)
Prostate	0.70 (0.14)
Bladder	0.64 (0.16)
Rectum	0.63 (0.16)

Abbreviations: DSC = Dice similarity coefficient; SD = standard deviation.

Voxelwise Conversion

- Ultrashort echo time imaging (UTE)
- No contribution of cortical bone in imaging



J. H. Jonsson, et al., Radiother Oncol **108**, 118-122 (2013).

Voxelwise Conversion

- Ultrashort echo time imaging (UTE)
- No contribution of cortical bone in imaging
- Intracranial < 0.5%

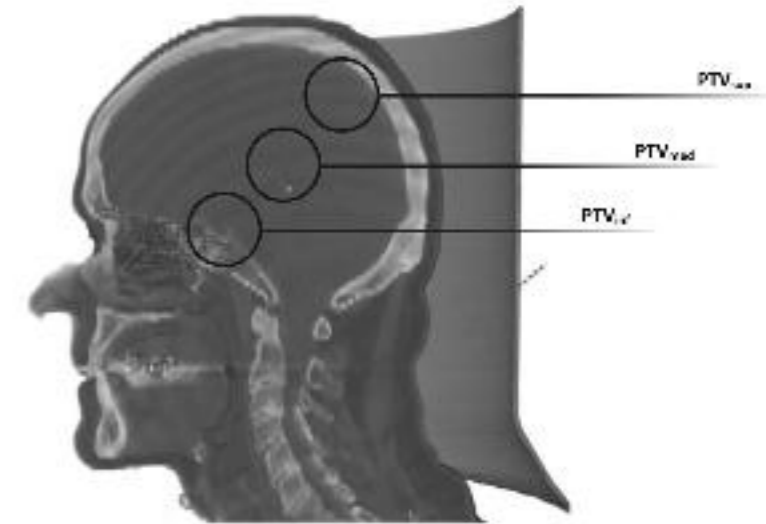


Fig. 1. The placement of the 3 spherical target volumes used in the study.

Table 3

Results from the treatment planning study summarized as the mean percentage point deviation from the CT calculation for each target and image data set over all 5 patients. The gamma index is presented as a mean percentage over all patients.

Target	Data	Isocenter [pp]	D(90) [pp]	V(100) [pp]	Gamma index%		
					3%/3 mm	2%/2 mm	1%/1 mm
PTV _{inf}	SCT	0.41	0.86 ^a	15.41	97.67	89.29	67.86
	Water	1.62	2.65 ^b	46.40 ^a	87.23	47.23	20.85
	Bulk	0.00	0.42	6.23	98.18	91.19	68.01
PTV _{med}	SCT	0.10	0.23 ^a	8.87	97.70	88.74	71.90
	Water	2.59 ^b	2.51 ^b	50.19 ^a	93.00	53.60	22.01
	Bulk	-0.20	0.17	-1.49	98.34	90.41	69.77
PTV _{sup}	SCT	0.40	0.10	6.41	97.92	88.22	67.61
	Water	2.71 ^b	2.11 ^b	31.79 ^b	88.41	42.66	16.82
	Bulk	-0.60	-0.69	-12.42	98.37	88.46	64.42

^a Significant at the 1% level.

^b Significant at the 0.1% level.

J. H. Jonsson, et al., Radiother Oncol **108**, 118-122 (2013).

Voxelwise Conversion

- Voxelwise conversion, sCT
- Ultrashort echo time imaging (UTE)
- Dual model, Prostate < 0.5%

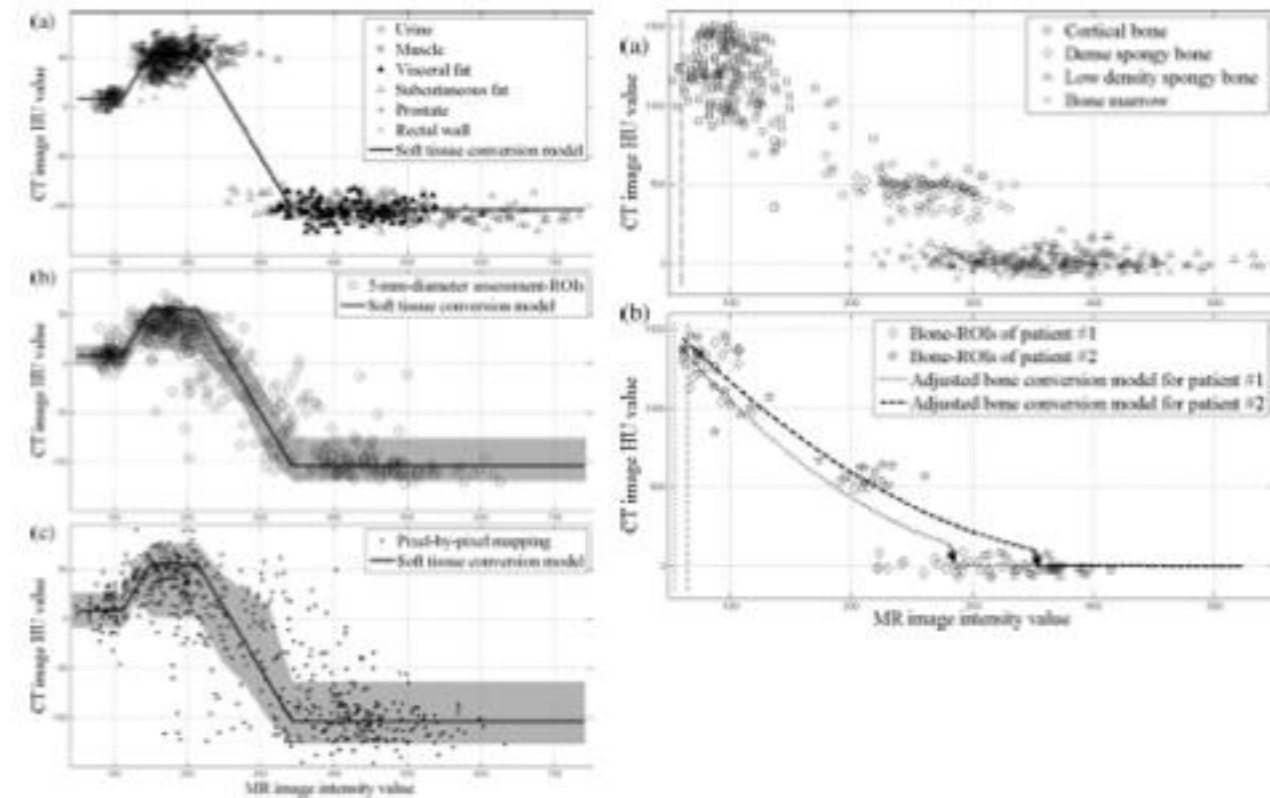


TABLE III. Absolute value deviations in PTV DVH-parameters between RTP images as averages with \pm SDs [and ranges] of the test patients.

Plan	PTV volume (%)	CT vs Pseudo (dual model) (%)	CT vs Pseudo (bones only) (%)	t - and F-tests ^a (p_t / p_F)	Pseudo (dual model) vs pseudo (bones only) (%)
IMRT	95	0.3 \pm 0.2 [0.1–0.7]	0.8 \pm 0.7 [0.2–2.2]	0.01/0.05	0.8 \pm 0.5 [0.0–1.5]
	50	0.3 \pm 0.2 [0.0–0.7]	0.9 \pm 0.7 [0.1–2.3]	0.00/0.04	0.8 \pm 0.6 [0.0–1.6]
	5	0.3 \pm 0.2 [0.0–0.7]	0.8 \pm 0.7 [0.0–2.4]	0.02/0.02	0.8 \pm 0.5 [0.0–1.7]
VMAT	95	0.3 \pm 0.2 [0.0–0.7]	0.5 \pm 0.4 [0.1–1.3]	0.89/0.04	0.4 \pm 0.2 [0.0–0.6]
	50	0.3 \pm 0.2 [0.0–0.8]	0.7 \pm 0.6 [0.0–2.0]	0.05/0.02	0.6 \pm 0.4 [0.2–1.4]
	5	0.3 \pm 0.3 [0.0–0.8]	0.7 \pm 0.7 [0.1–2.2]	0.05/0.02	0.7 \pm 0.4 [0.1–1.4]

^aStatistical tests were conducted to deviations (including signs) in DVH parameters by comparing the deviations between CT and the dual model HU conversion pseudo-CT image with the deviations between CT and bones-only HU conversion pseudo-CT image.

J. Korhonen, et al., Med Phys 41, 011704 (2014).

Conventional Direct Conversion Methods

- Brain and prostate
- Bulk density, <3% in the target
- Recent techniques, <1% in the target

Table Selection of Presented Dosimetric Results for MR-Based Dose Calculations

References	Method	Region	#*	Difference†	Quantification Parameter
Lee et al ¹⁵	Bulk density assignment	Prostate	4	<2.0%	Volume within 60%, 70%, 80%, and 90% isodose levels
Chen et al ³²	Nonheterogeneity corrected	Prostate	15	<2.0%	D95 of prostate volume
Chen et al ⁴	Nonheterogeneity corrected	Prostate	15	<2.0%	Isocenter point dose
Prabhakar et al ⁷	Nonheterogeneity corrected	Brain	25	< ±1.9%	Mean dose to target volume
Kristensen et al ¹⁸	Bulk density assignment	Brain	11	0.4 ± 0.3%	Isocenter point dose
Eilertsen et al ¹⁹	Bulk density assignment	Prostate	10	<0.5%	Mean dose to CTV
Jonsson et al ¹⁷	Bulk density assignment	Prostate	10	0.2% ± 0.5%	Monitor units to reach prescribed isocenter point dose
Jonsson et al ¹⁷	Bulk density assignment	Thorax	10	0.2% ± 0.4%	Monitor units to reach prescribed isocenter point dose
Lambert et al ¹³	Bulk density assignment	Prostate	39	1.6% ± 0.8%	ICRU point dose
Dowling et al ⁹	Atlas conversion	Prostate	37	<2.0%	Isocenter point dose
Kapanen and Tenhunen ⁸	Direct conversion of bones and density-assigned soft tissue	Prostate	10	< ±1.3%	Dose for all points within PTV
Jonsson et al ²⁸	Direct conversion	Brain	5	0.4%	Mean isocenter point dose

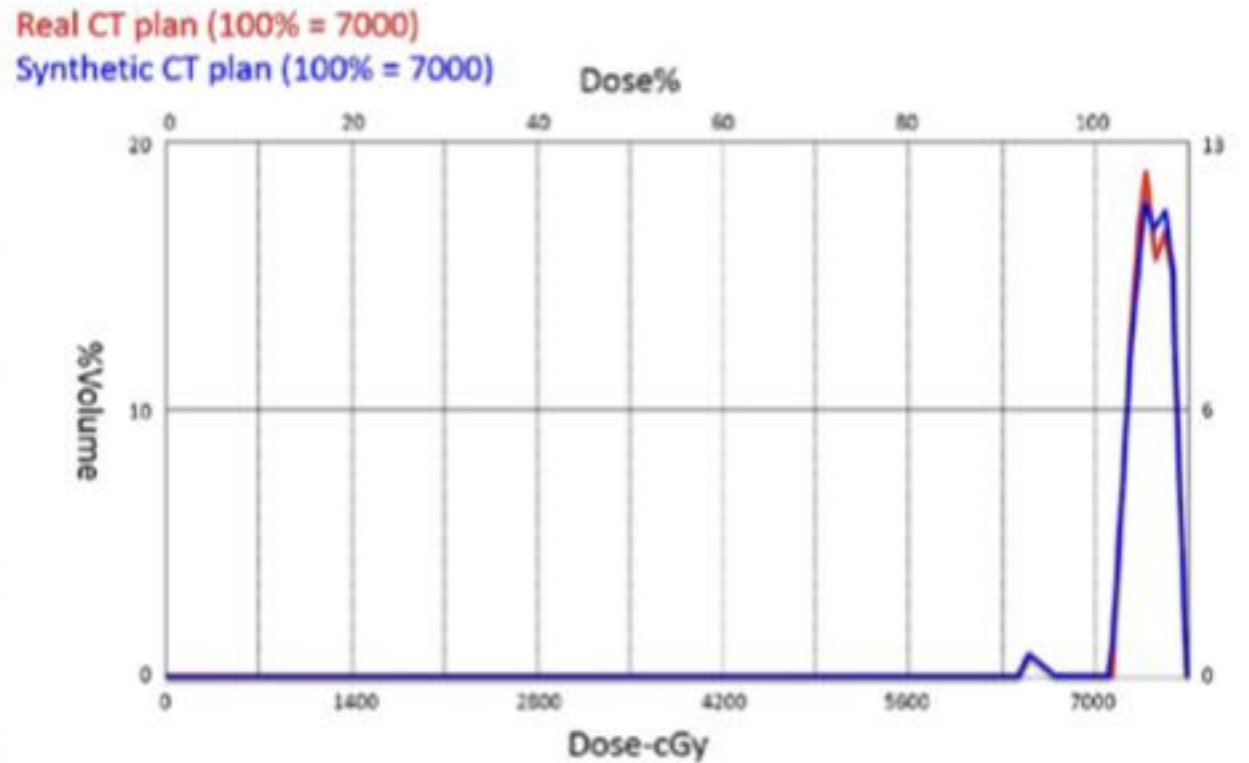
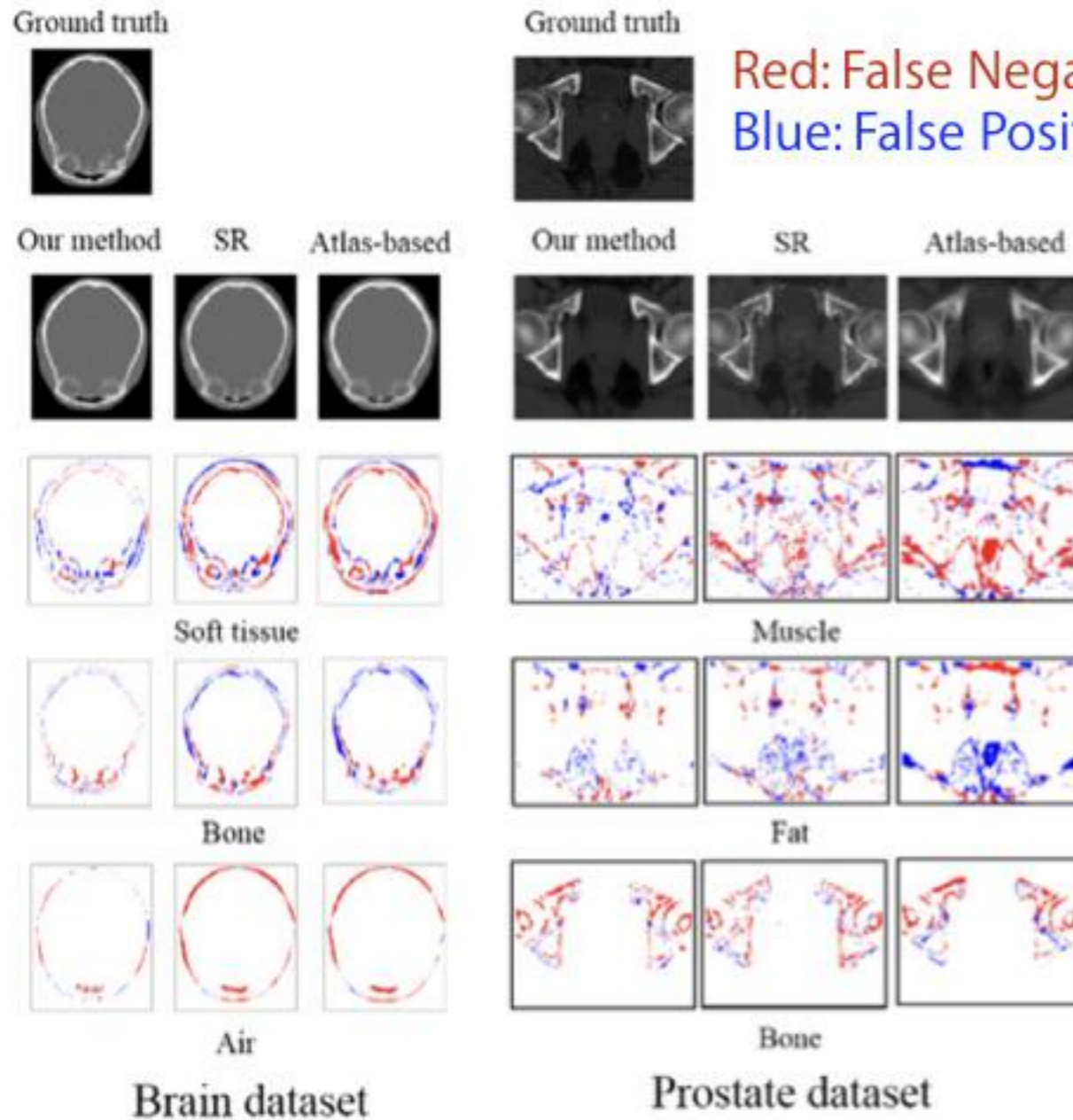
CTV, clinical target volume; ICRU, International Commission on Radiation Units and Measurements, PTV, planning target volume.

*Number of patients.

†Difference compared with clinical treatment planning.

Machine-Learning based synthetic CT

- Factors which can affect accuracy could be overcome using machine-learning from big-data sets.



Tri Huynh, et al., IEEE Trans MED Imaging 35 (1) (2016).

Challenge: Four-Dimensional MR

Cine-MRI

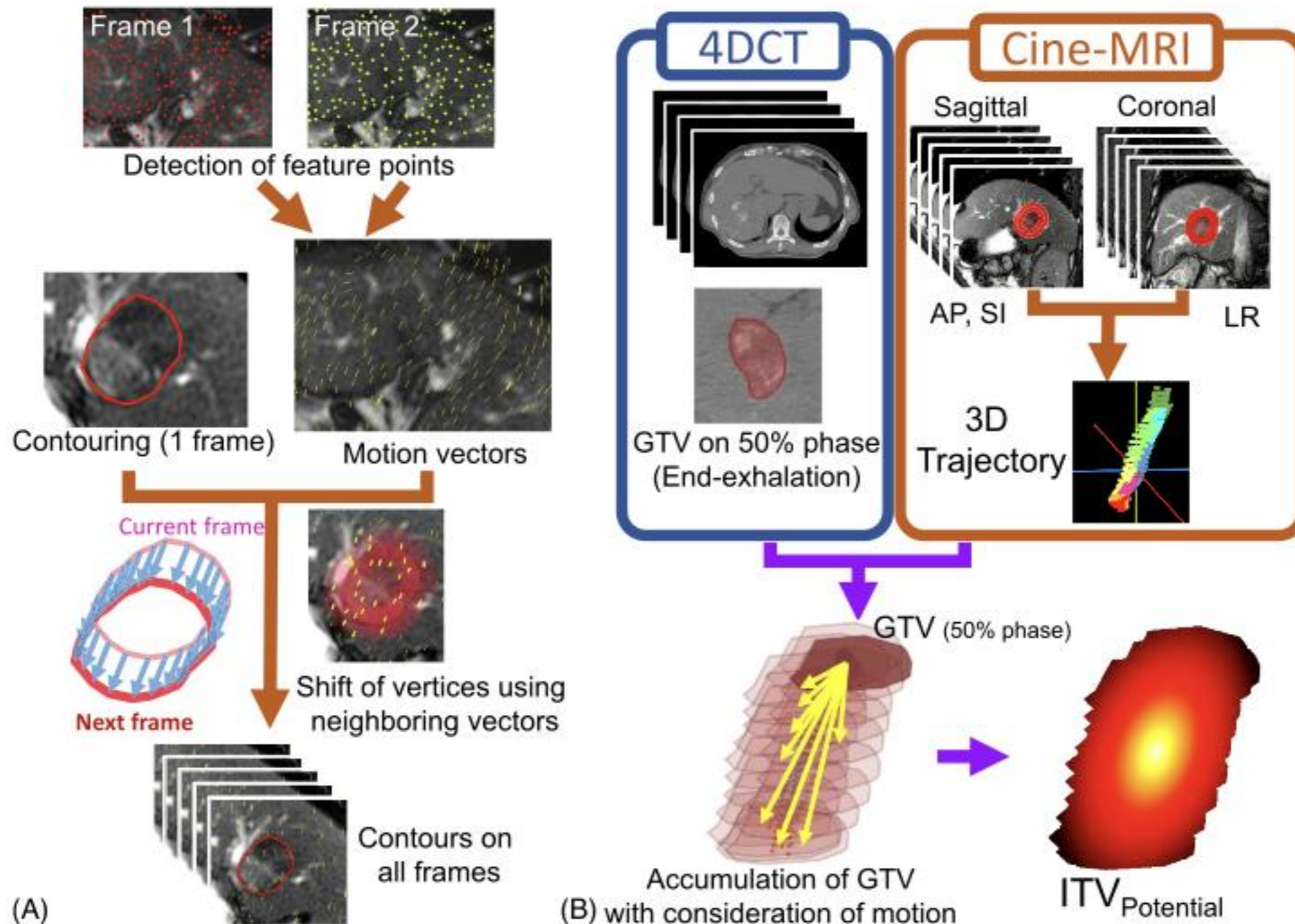
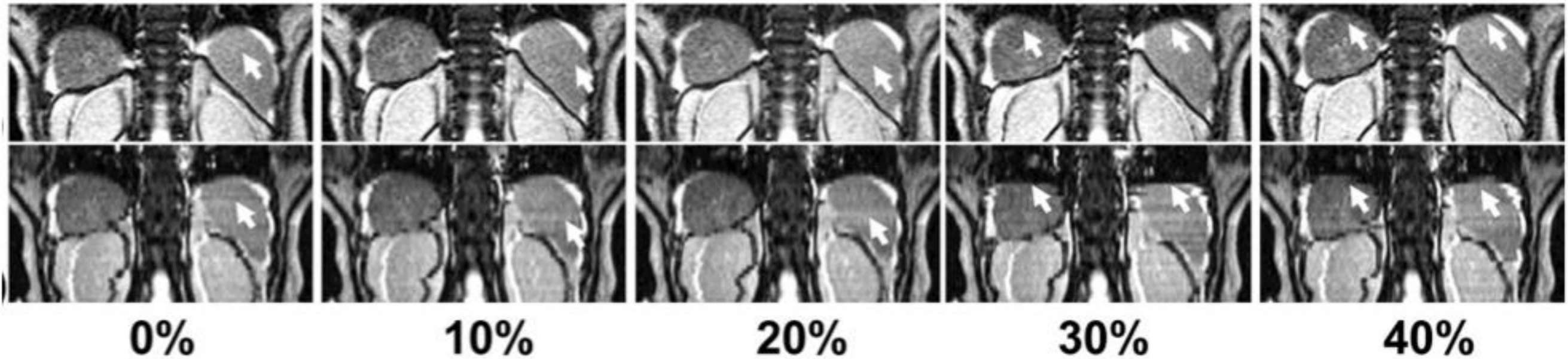
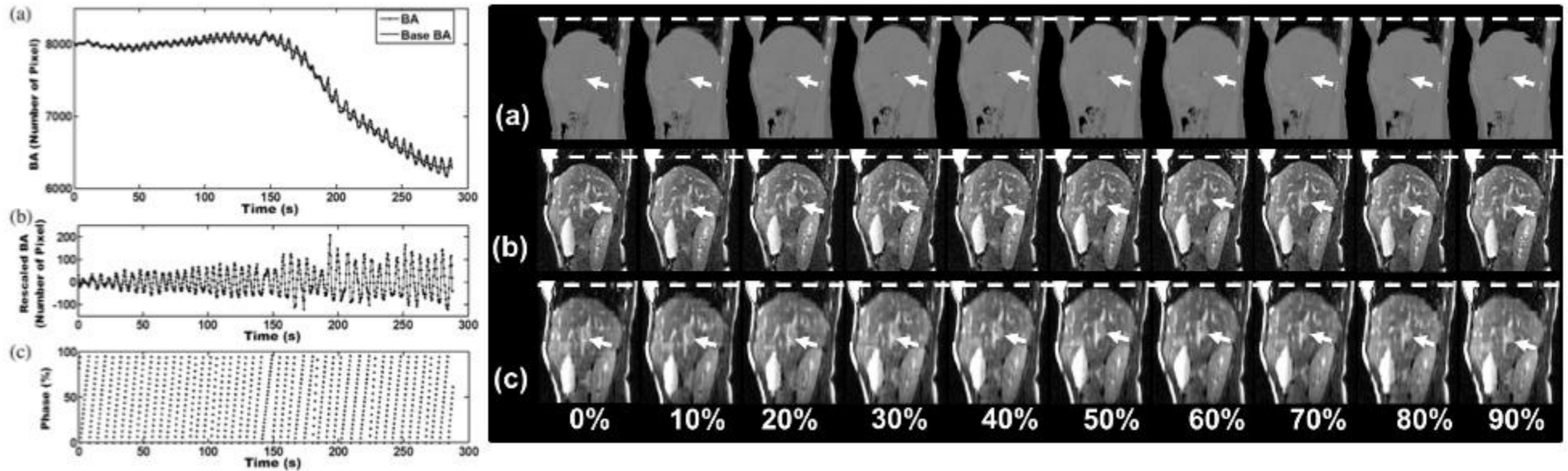


FIG. 1. A flowchart of the (A) automatic estimation of tumor motion on cine-MRI images and (B) calculation of potential ITV (ITV_{Potential}) using GTV delineated on 4DCT and motion data derived from orthogonal cine-MRI images. Abbreviation: LR, left–right; AP, anterior–posterior; SI, superior–inferior.

Y. Akino, et al., Med Phys **41**, 111704 (2014).

Body Area with 2D Axial Image



J. Yang, et al., Int J Radiat Oncol Biol Phys **88**, 907-912 (2014).

Navigation Slice

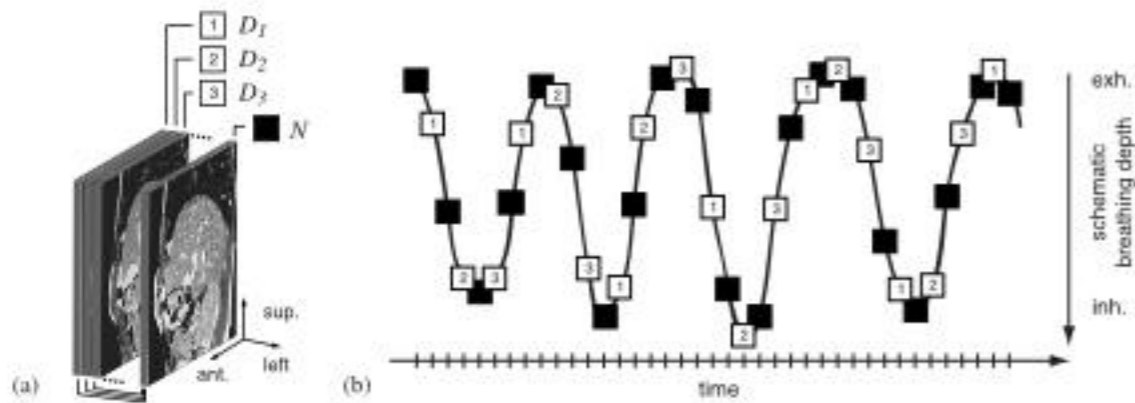
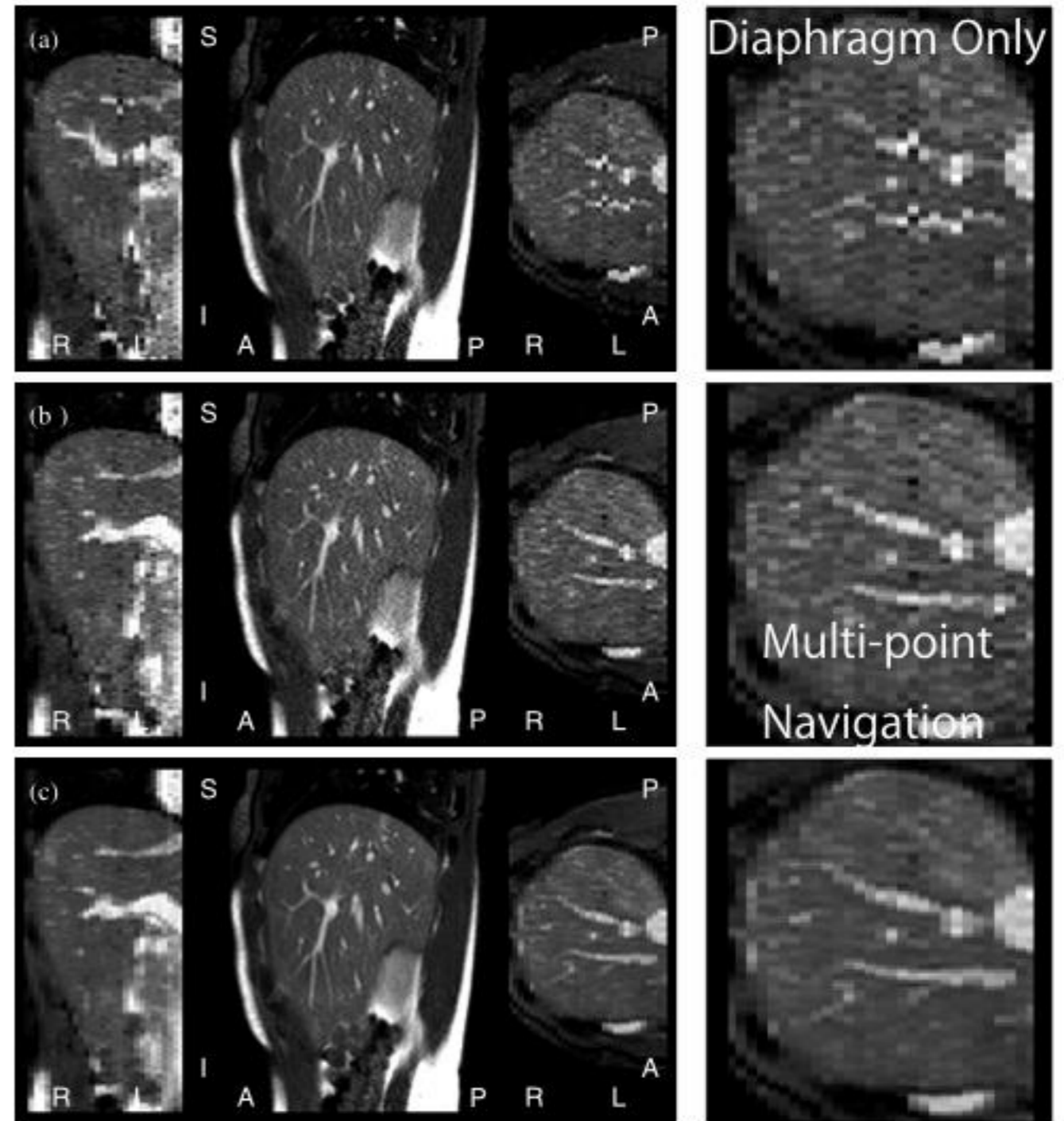
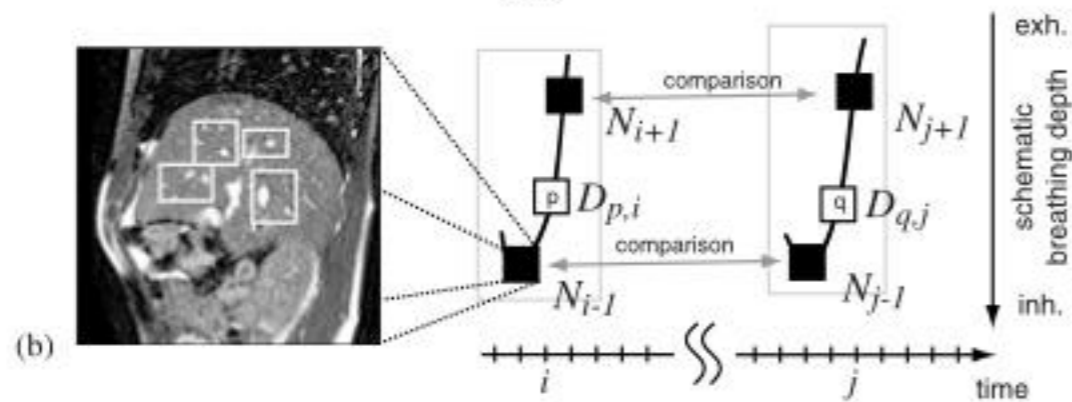
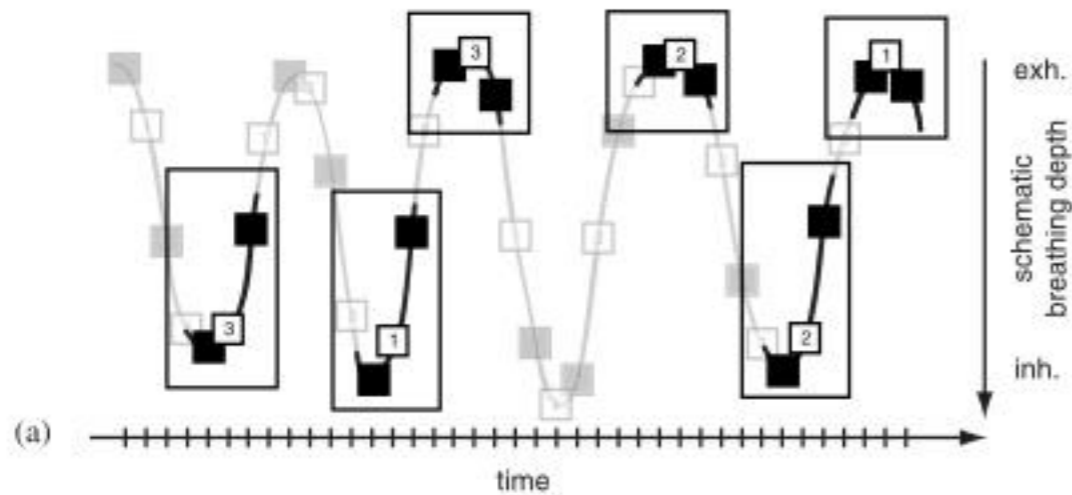


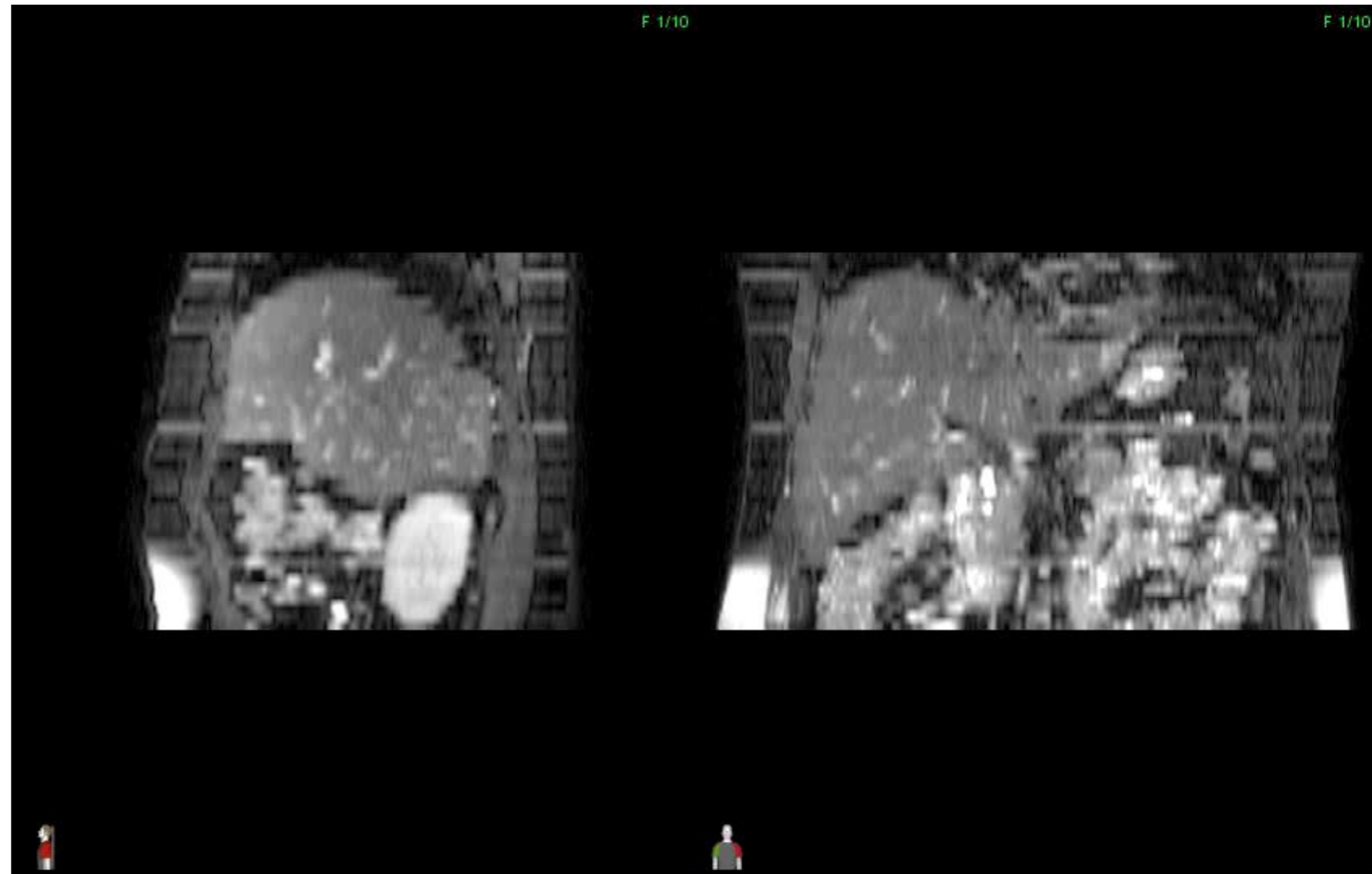
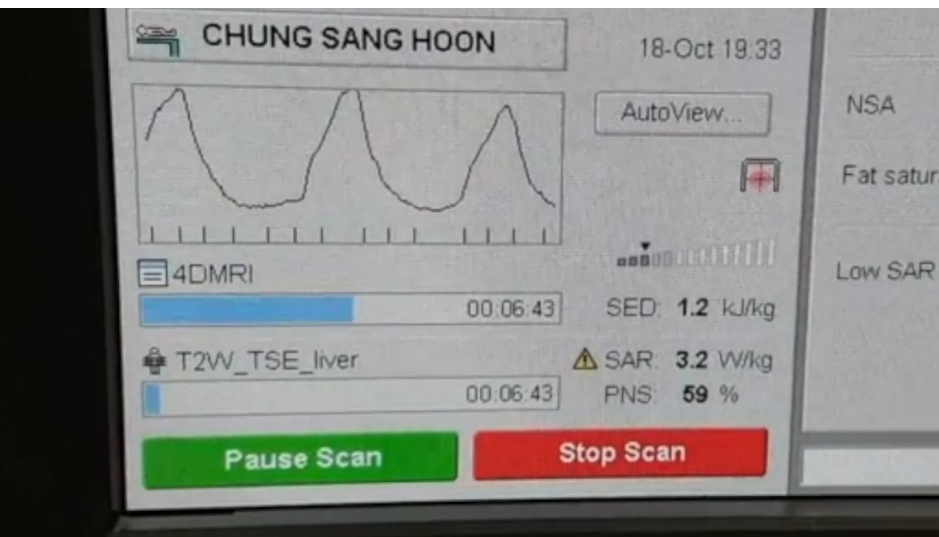
Figure 1. (a) Sagittal slices covering the volume of interest. One dedicated slice N is used as navigator slice for image sorting. (b) Interleaved acquisition of data and navigator frames.



M. von Siebenthal, Phys Med Biol **52**, 1547-1564 (2007).

Our experience

- Physiology signal was used as like 4DCT using RPM.
- However, the axial image were acquired prospectively.

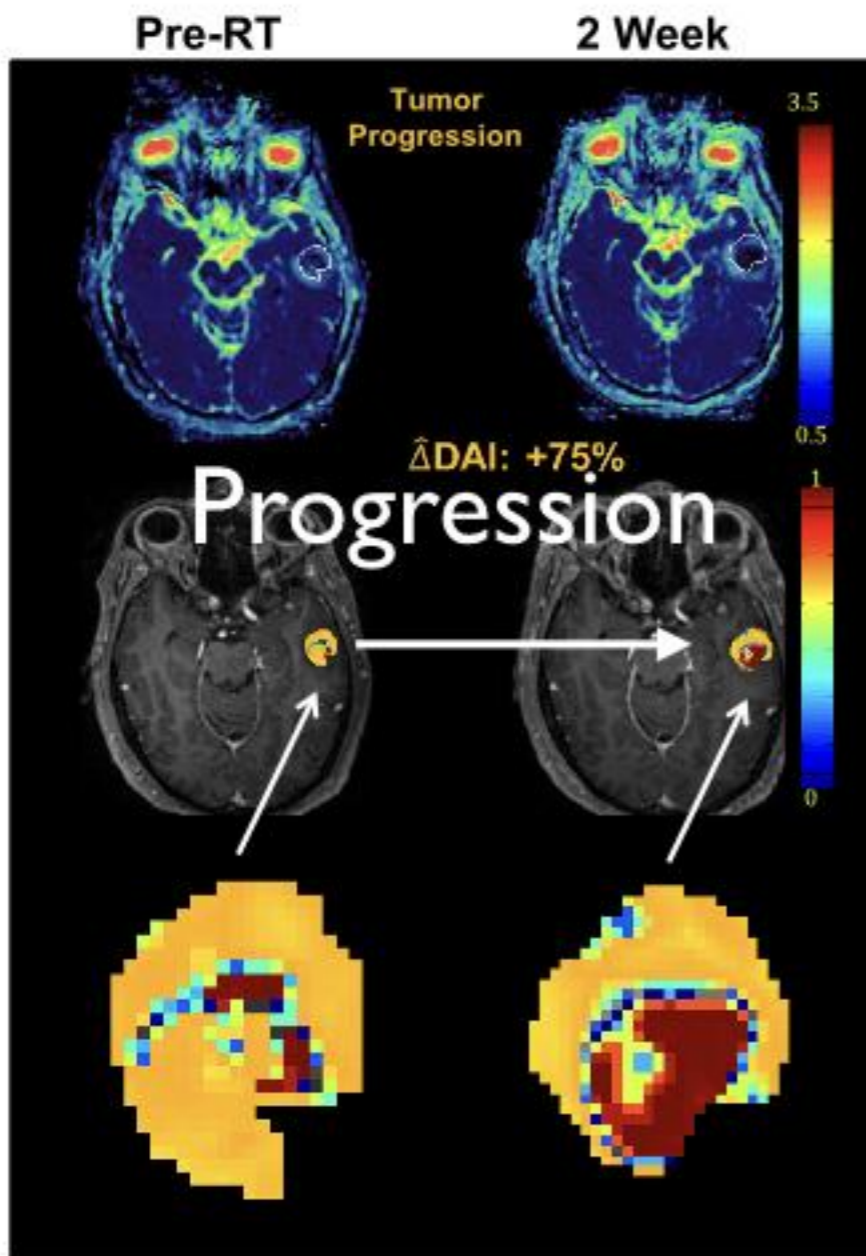


Challenge: Response Evaluation

Response Evaluation

- Role of Diffusion MRI in radiotherapy
 - Mobility of water within tissue at the cellular level without the need of any exogenous contrast agent
 - A sensitive marker for alterations in tumor cellularity and the early assessment of treatment response.
- ADC (Apparent Diffusion Coefficient)
 - DWI acquired with 2 (or more) b-values reflect the local mobility of water molecules calculated on a pixel-by-pixel basis
- DAI (Diffusion Abnormality Index)
 - A diffusion abnormal probability accounting for both of these changes was generated for each tumor voxel and then summed altogether

DAI and DWI



Diffusion abnormality index (DAI) of a patient with a brain metastasis treated with whole-brain radiation therapy. DW-MRI was obtained both pre-RT (left column) and post-RT (right column). Top row: color-coded ADC maps, middle row: DAI maps, and bottom row: zoomed DAI maps of the tumor. The tumor volume showed no significant change between pre-RT and post-RT. However, the DAI increased by 75% from pre-RT to post-RT, suggesting tumor progression which was confirmed by post-Gd T1-weighted MRI 1 month post-RT.



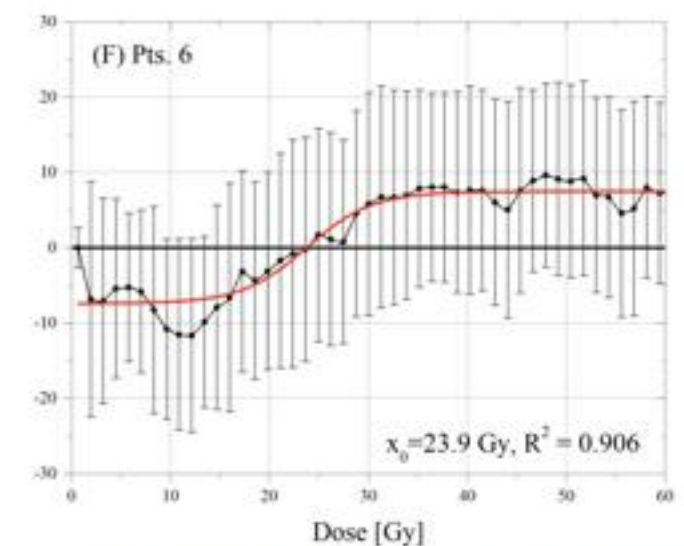
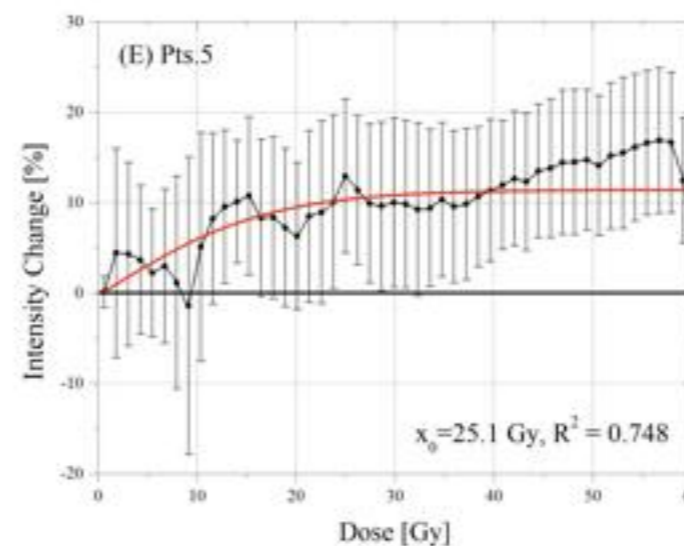
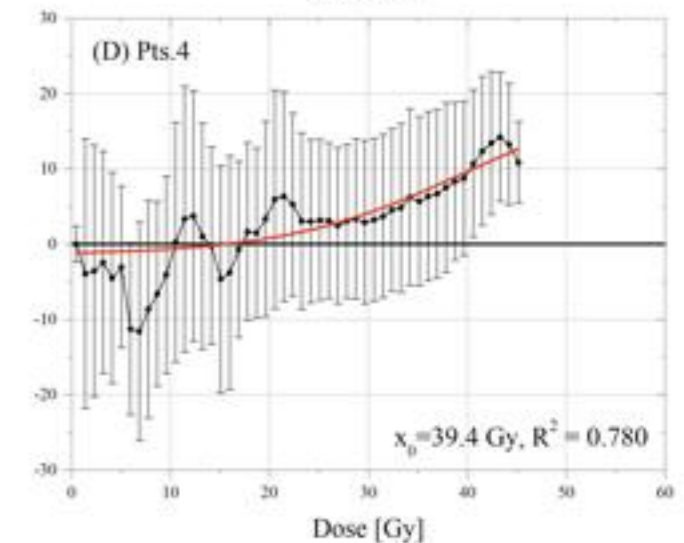
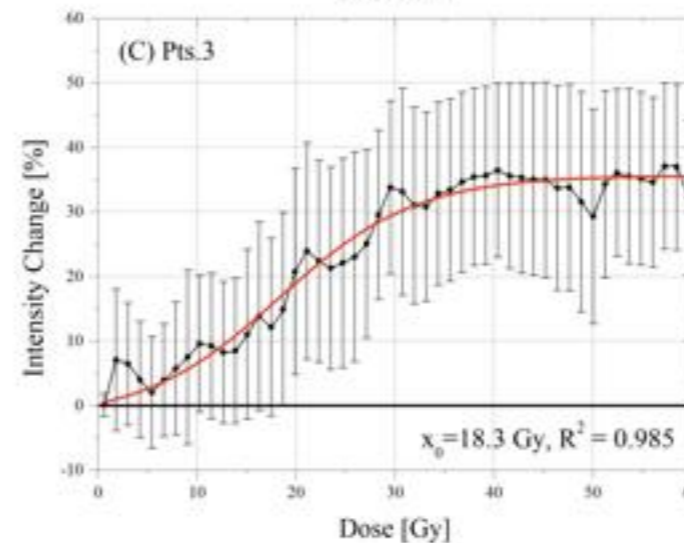
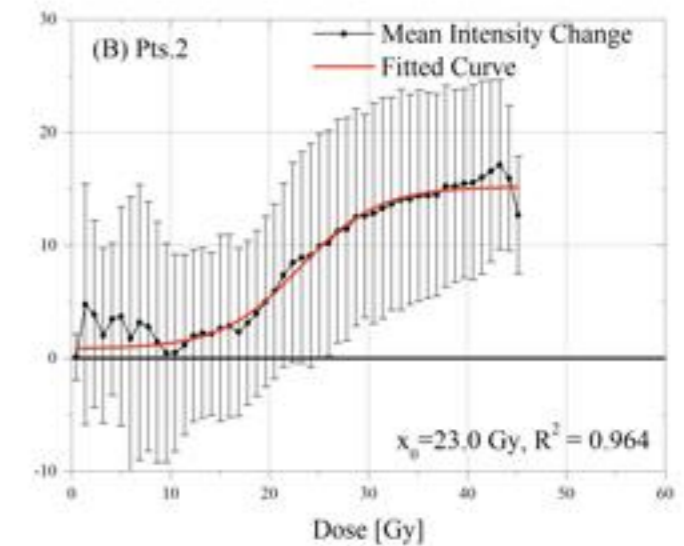
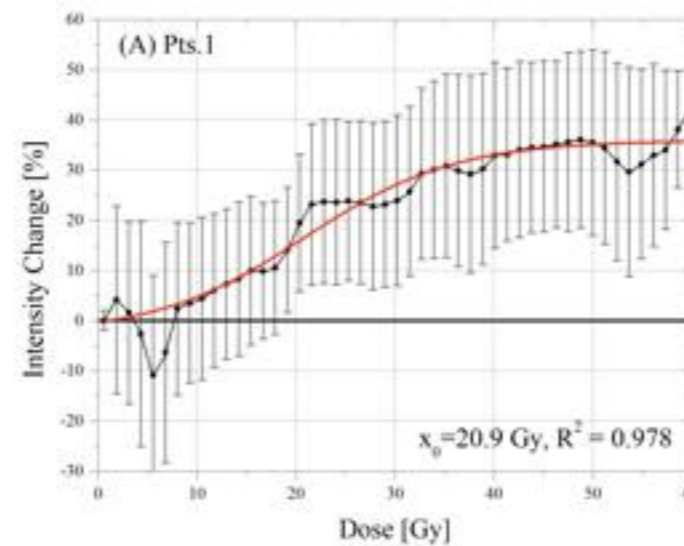
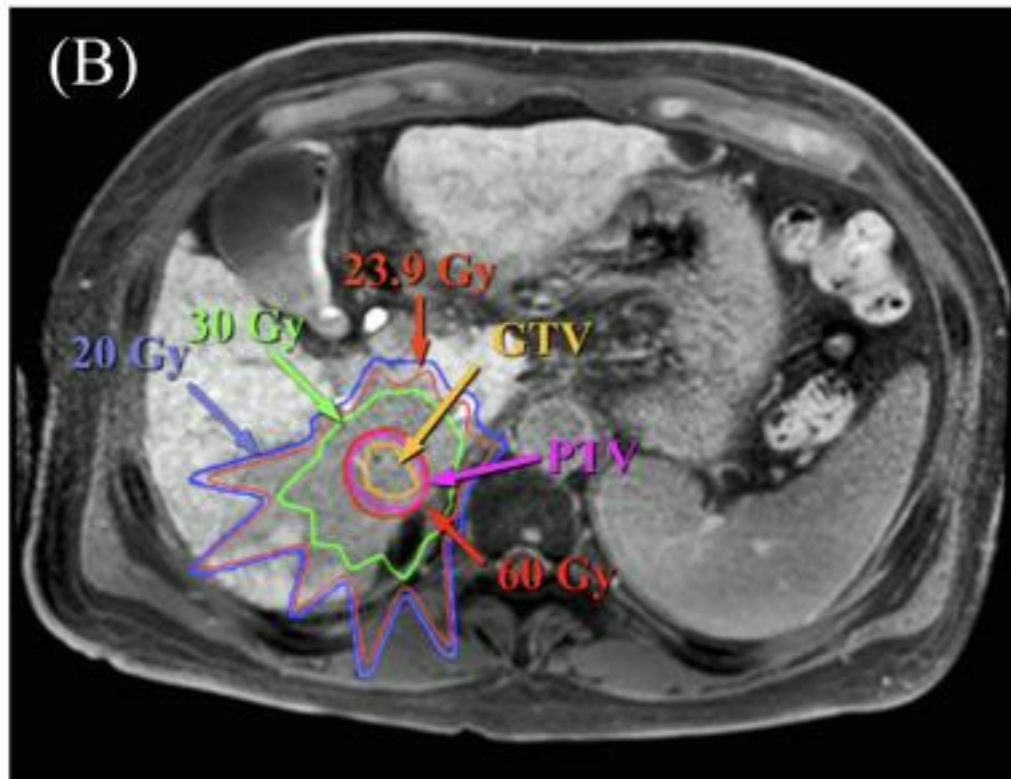
Region of interest (ROI) drawing on an apparent diffusion coefficient (ADC) map. Two radiation oncologists measured ADC values of target hepatocellular carcinoma (HCC) in reference to other diffusion images.

J. I. Yu, et al., Red Journal **89**, 814-821 (2014).

R. Farjam, et al., Practical radiation oncology **3**, S5 (2013).

Normal Tissue Damage

- Radiation-induced hepatocytes injury
- Hepatobiliary phase images of Promovist enhanced MRI
- Correlation of dose to changes in signal intensity between pretreatment and follow-up MRI



Estimation of Normal Liver Function

Quantitative signal intensity

$$ER-SI-s = \frac{(SI_{liver}/SI_{spleen})_{post} - (SI_{liver}/SI_{spleen})_{pre}}{(SI_{liver}/SI_{spleen})_{pre}} \quad (2)$$

$$ER-SI-m = \frac{(SI_{liver}/SI_{muscle})_{post} - (SI_{liver}/SI_{muscle})_{pre}}{(SI_{liver}/SI_{muscle})_{pre}} \quad (3)$$

$$ER-SI-c = \frac{(SI_{liver}/[SS \cdot RSS])_{post} - (SI_{liver}/[SS \cdot RSS])_{pre}}{(SI_{liver}/[SS \cdot RSS])_{pre}} \quad (4)$$

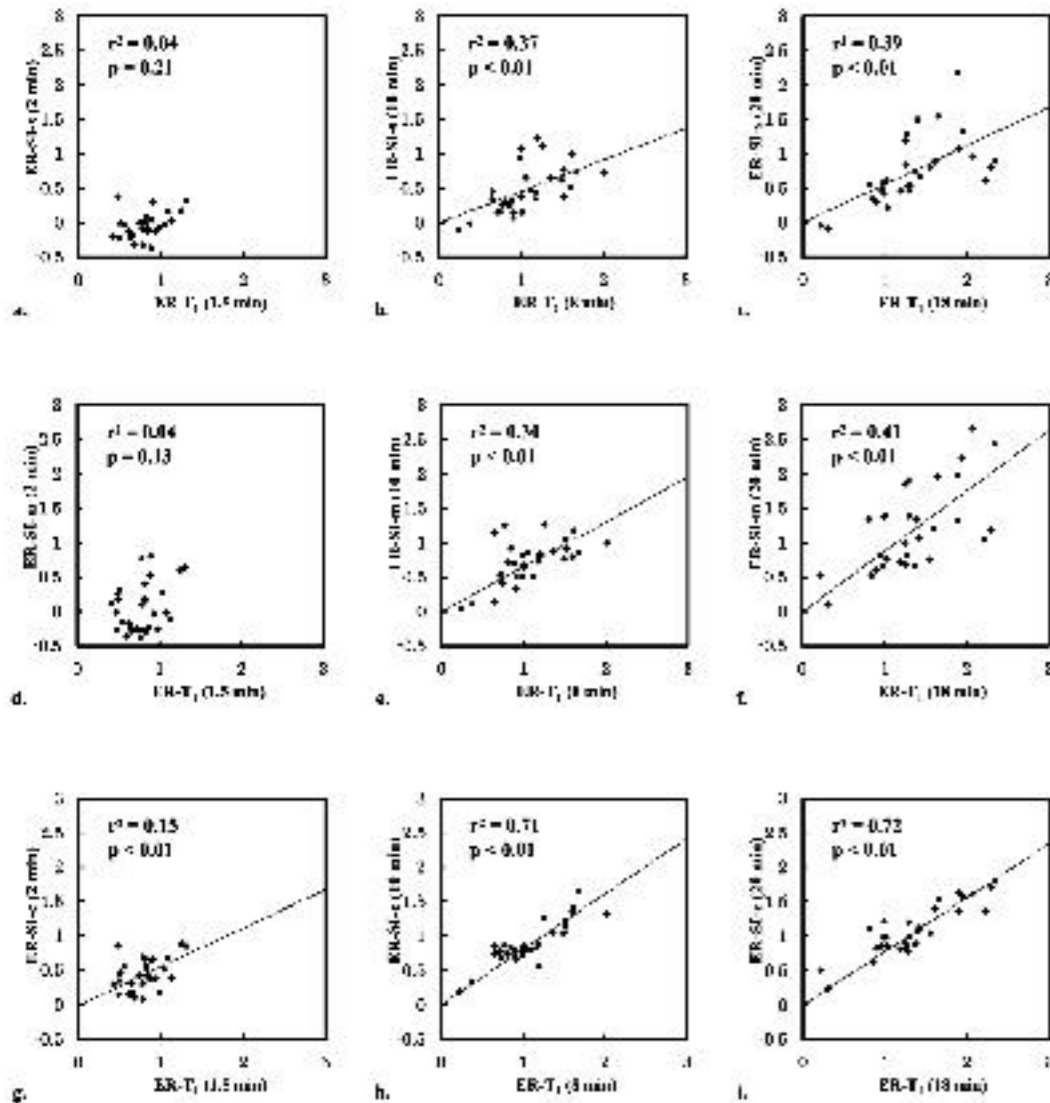


Fig. 3. Graphs showing the correlation of ER-T₁ with ER-SI-s (a)-(c), ER-SI-m (d)-(f), and ER-SI-c (g)-(i) determined by linear regression analysis (a, d, g) for all 30 patients. Comparison of ER-T₁ at 1.5 min and ER based on signal intensity (SI) 2 min after Gd-EOB-DTPA administration (b, e, h). Comparison of ER-T₁ at 8 min and ER based on SI 10 min after administration (c, f, i). Comparison of ER-T₁ at 18 min and ER based on signal intensity 20 min after administration. Dotted lines are the regression lines.

Contrast agent specific T1 relaxometry

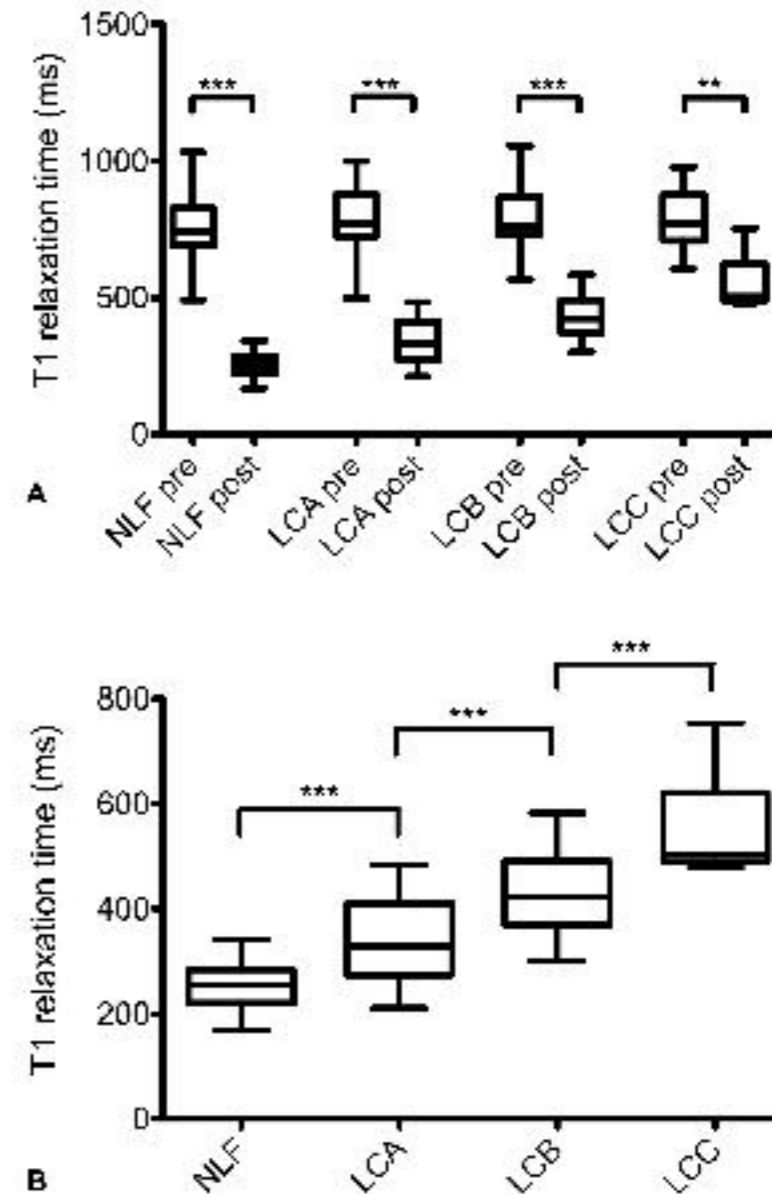


Figure 1. Pre- and post-contrast T1 relaxation times. (A) Boxplots indicating T1 relaxation times before (pre) and after (post) Gd-EOB-DTPA administration in patients with normal liver function and in patients with liver cirrhosis Child-Pugh A, Child-Pugh B, and Child-Pugh C. After contrast medium administration, T1 relaxation times were significantly reduced in each group. (B) Boxplots indicating T1 relaxation times after Gd-EOB-DTPA administration in patients with normal liver function and in patients with liver cirrhosis Child-Pugh A, Child-Pugh B, and Child-Pugh C. T1 relaxation times increased significantly with increased progression of liver cirrhosis. NLF: normal liver function; LCA: liver cirrhosis Child-Pugh A; LCB: liver cirrhosis Child-Pugh B; LCC: liver cirrhosis Child-Pugh C. Data given as mean T1 reduction rate \pm standard deviation. Tukey's adjustment was used to generate Boxplots, and the Wilcoxon-Test was used to compare groups.

Challenge: MR-Guided RT

MRgRT

- MRgRT in Princess Margaret Cancer Centre
- 1.5T MRI based external radiotherapy and brachytherapy

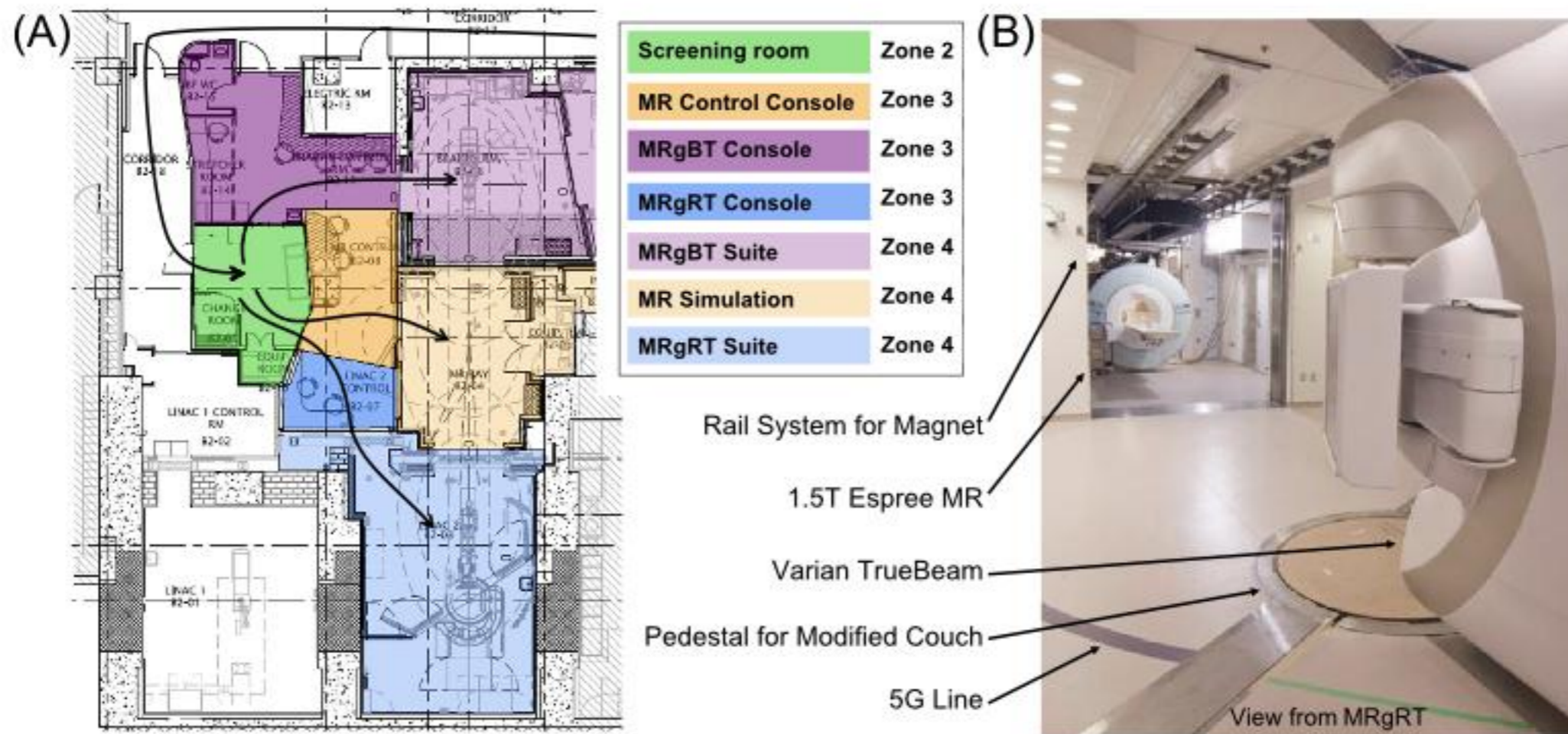
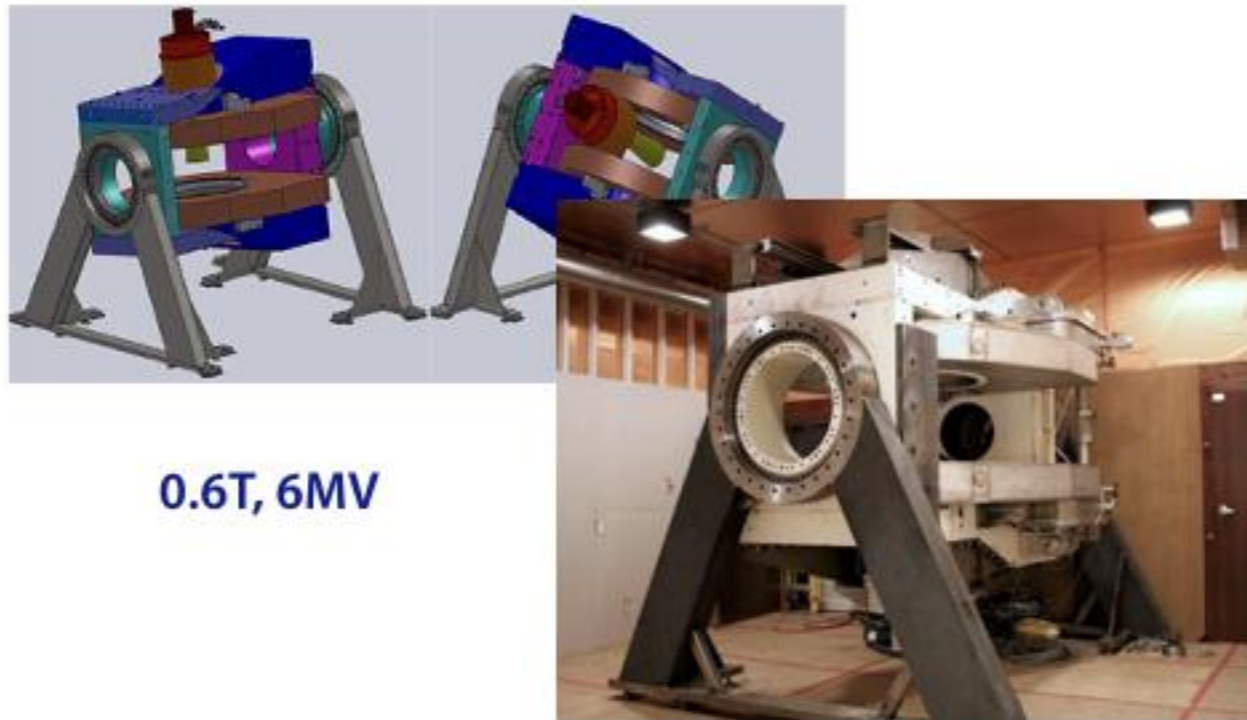


Figure (A) Floor plan and safety zones of the MR-guided RT facility at the Princess Margaret Cancer Centre showing brachytherapy, imaging, and external-beam RT suites. (B) Photograph of the accelerator and MR scanner in the facility. The magnet is advanced on the rail system into the MRgRT suite, and the patient is positioned via a modified treatment couch. At nearest approach, the magnet to linear accelerator isocenter distance is 3.1 m.

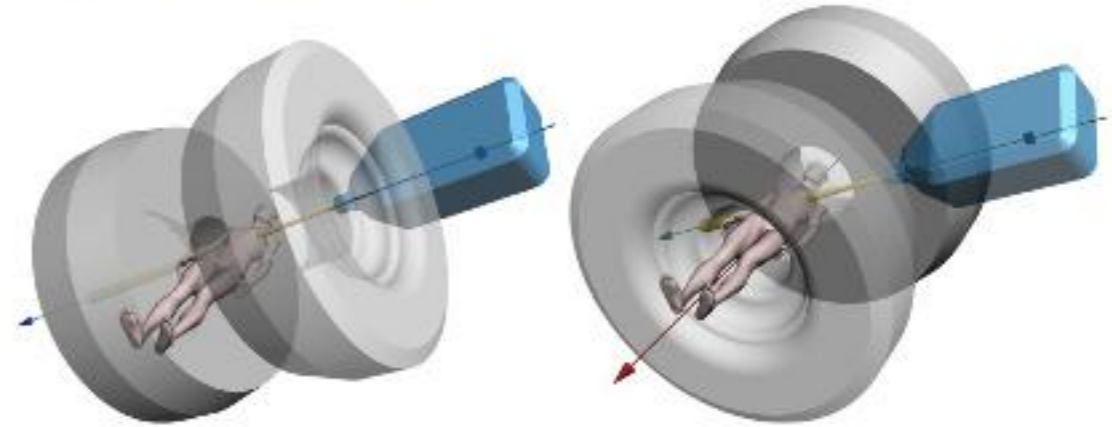
Challenges: Rotating biplanar linac

Cross Cancer Institute, University of Alberta,
Edmonton, Alberta, Canada.

Sydney Medical School, The University of Sydney, New
South Wales, Australia.



0.6T, 6MV



1.0T, 6MV

Figure 1 (Left) The inline orientation, that is, linac aligned with B_0 . (Right) The perpendicular orientation, that is, linac perpendicular to B_0 . Both the orientations are to be experimentally investigated. (Adapted with permission from Constantin et al.³) (Color version of figure is available online.)

Table 2 A Comparison of the Advantages of the Inline and the Perpendicular Approaches that Will be Experimentally Investigated

Advantages of the Inline Approach (Fig. 1, Left)	Advantages of the Perpendicular Approach (Fig. 1, Right)
No beam attenuation and Compton scatter to the patient from irradiation through the cryostat (if closed bore)	More similar design to mass-produced conventional MRI systems (if closed bore)
Less effect of the B field on electron gun operation	Lower constraints on magnet, gradient coil, and RF design, resulting in higher potential imaging performance and higher B field (if closed bore)
Less effect of the B field on waveguide operation	Lower skin dose
Less effect of the B field on electron transport within the patient: sharper penumbra and no electron return effect	No need to rotate the magnet or the patient
Lower exit dose	
Linac fixed with respect to the magnet. This reduces the need to manage eddy currents or dynamic shimming requirements, where the linac moves with respect to the magnet	

Abbreviation: RF, radiofrequency.

Challenges: MRI with linac

- UMC Utrecht, Utrecht, The Netherlands.
- 1.5T MRI and 6MV (Philips and Elekta)
- Installation started at June 12, 2014

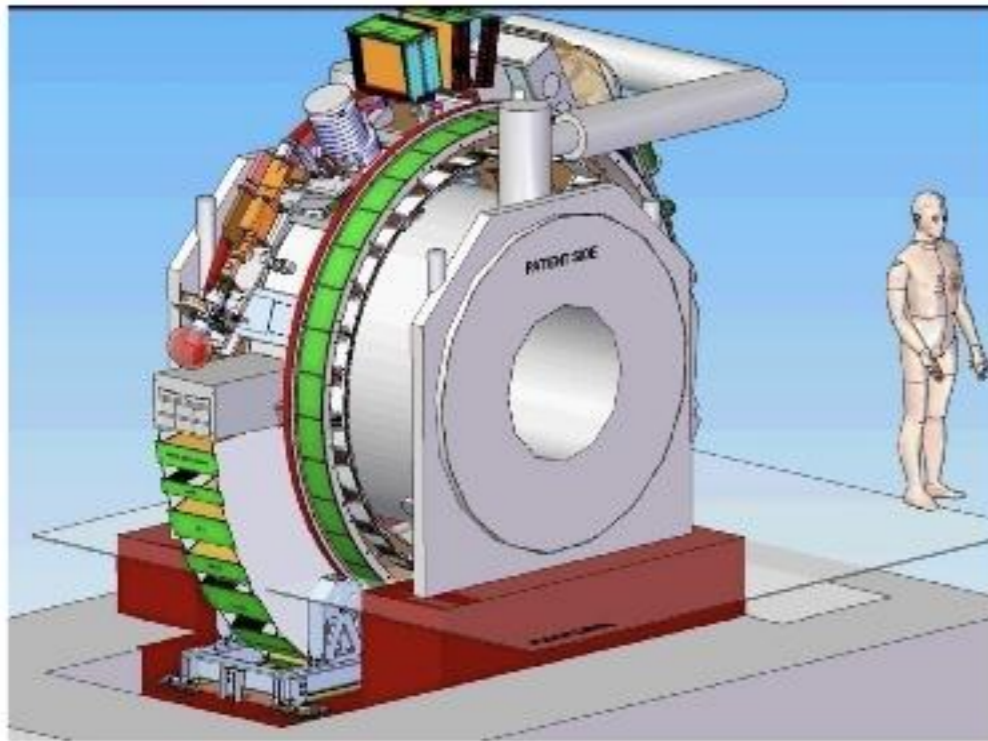


Figure 2 Schematic design of the combined MRI-linac system. (Color version of figure is available online.)

S. Crijns and B. Raaymakers, "From static to dynamic 1.5T MRI-linac prototype: impact of gantry position related magnetic field variation on image fidelity," *Phys Med Biol* **59**, 3241-3247 (2014).

MRI-Linac

- Canada, Australia, and Netherland (USA)
- Realtime imaging with higher contrast and resolution
- Clinical effectiveness - Being validated
- Technical aspects - Potential benefits

Table 1

Authors	Jaffray et al	Mutic et al	Fallone	Keall et al	Legendijk et al
Field strength (Tesla)	1.5	0.35	0.56	1	1.5
Radiation source	6 MV	Co-60	6 MV	6 MV	6 MV
In-line imaging	No	Yes	Yes	Yes	Yes
Clearance	70-cm bore	70-cm bore	85-cm open bore	82-cm open bore	70-cm bore
Install requirement	Adjacent MRI suite	Conventional bunker	Conventional bunker	Conventional bunker	Conventional bunker

MRIdian

- 0.35T MRI, 70 cm bore, 6MV FFF Beam linac, 1100 MU/min
- 27.4 cm x 24.1 cm
- Conventional (3D), IMRT, and SBRT delivery
- 4 FPS (8 FPS)

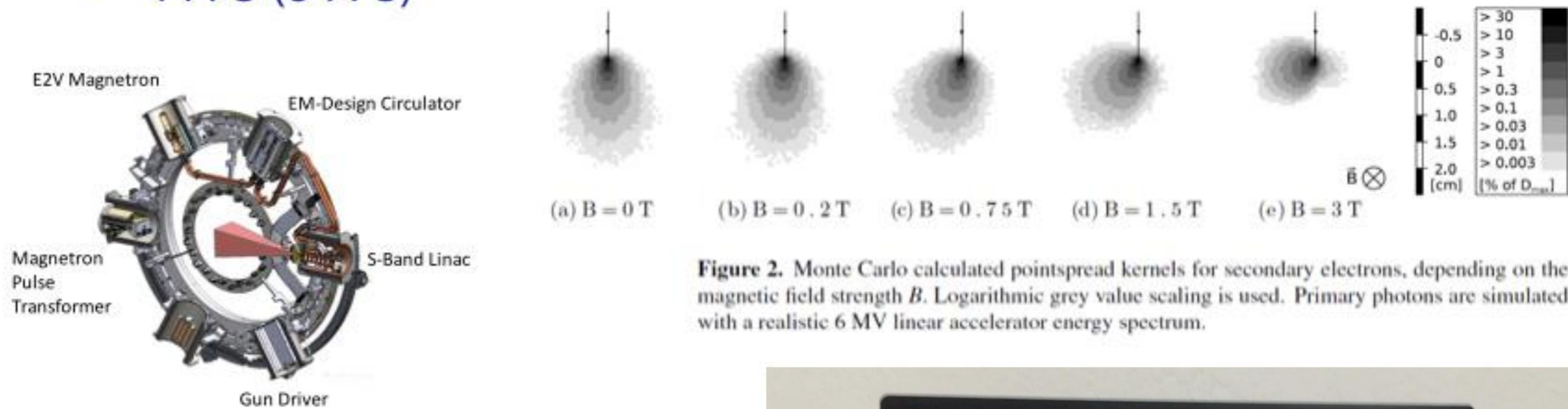
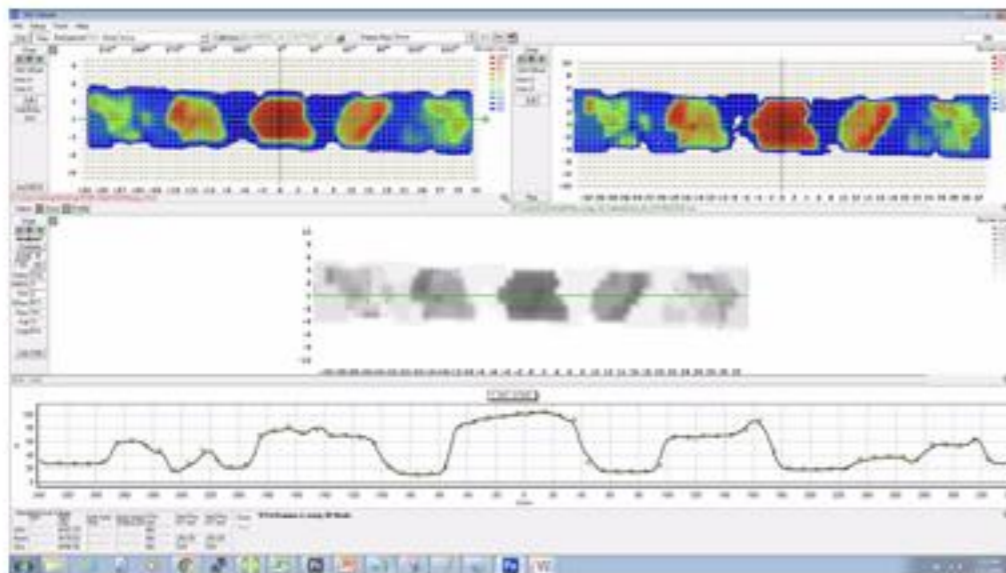


Figure 2. Monte Carlo calculated pointspread kernels for secondary electrons, depending on the magnetic field strength B . Logarithmic grey value scaling is used. Primary photons are simulated with a realistic 6 MV linear accelerator energy spectrum.



Courtesy of Justin C Park

Summary

- Use of MRI in RT process could increase accuracy of delineation of target volume, and could be reduce complication of normal organs due to reduction of irradiated volume potentially.
- Integration of MRI into Treatment Planning
 - Dose discrepancy in MR based treatment planning could shows good agreement with less than 1%.
 - MR simulation should be established carefully: geometrical distortion due to magnetic field strength, RF coil etc
- Near future, MR-Only RT process including in-room image-guidance and real-time imaging could be established.

